Magnesium Doping for the Stabilization of a Spinel lithium Manganese Oxide for Lithium Recovery from Flowback and Produced Water

By

Fangshuai Wu

A thesis submitted in partial fulfillment of the requirements for the degree of

Master of Science

Department of Earth and Atmospheric Sciences

University of Alberta

Abstract

Flowback and produced water (FPW), a potentially hazardous byproduct of oil and gas production, is a complex mixture of dissolved salts and organic compounds. FPW often contains modest concentrations of lithium, from tens to hundreds of parts-per-million. For this reason, and in response to the rising global demand for lithium driven by the recent surge in the battery industry, FPW is being regarded as a potential source for lithium production. Among the various direct lithium extraction (DLE) approaches, spinel lithium manganese oxide (LMO) ion-sieves stand out as one of the most promising materials for lithium recovery from FPW due to their high lithium selectivity as well as high uptake. However, LMO ($Li_{1.6}Mn_{1.6}O_4$) experiences mass loss due to the reductive dissolution of manganese, which is a result of high concentrations of free electrons in FPW. Consequently, mass loss leads to structural degradation of the ion sieve, affecting its regeneration. To solve the problem of ion-sieve mass loss, we doped pristine LMO with different concentrations of magnesium by a solid-state method to synthesize magnesium-doped lithium manganese oxides, $Li_{1.6}Mg_xMn_{1.6-x}O_4$ or LMMO-x (where x = 0.1, 0.2, 0.3, 0.4). The lithium uptake in FPW decreases from 25.7 $mg \cdot g^{-1}$ for acid-treated LMO to 11.3 $mg \cdot g^{-1}$ for LMMO-0.4. Subsequent studies reveal that the kinetics of lithium adsorption of these ion-sieves follow a pseudo-second-order kinetic model, and LMMOs exhibit relatively slower lithium uptake rates. However, LMMOs retain 95% of their initial lithium uptake after the 5^{th} cycle of use, whereas LMO only maintains 90%, indicating that LMMOs are more stable and exhibit better reusability as a result of the magnesium doping. More importantly, during the acid desorption step to recover lithium, the average manganese loss decreases significantly from 3.19% for LMO to 0.73% for LMMO-0.4 because substitution of manganese by magnesium reduces the content of structural trivalent manganese. The mean oxidation states (Z_{Mn}) of manganese determined by a standard

oxalic acid method in conjunction with X-ray absorption near edge structure (XANES) spectra support the conjecture that doping magnesium into LMO leads to an increase of Z_{Mn}, resulting in improved structural stability. Combined transmission electron microscopy – electron energy loss spectroscopy (TEM-EELS) shows that homogeneous doping of magnesium in LMO makes it less susceptible to manganese reduction when exposed to FPW. Furthermore, extended X-ray absorption fine structure (EXAFS) spectra reveal that pristine LMO undergoes an irreversible structural contraction during regeneration, while such an effect is not observed in LMMOs. Our results show that LMMOs are promising candidates for scale-up to an economic DLE technology.

Acknowledgements

I would like to thank, first and foremost, my direct supervisor Dr. Daniel Alessi, for offering me the opportunity to work on this interesting project and for his support, advice and guidance during my MSc study. I would like to express my appreciation to Dr. Kurt Konhauser for admitting me to this program and for his professional and constructive feedback on the abstracts and posters presented at two conferences: the Geological Society of America (GSA) 2022 in Denver, Colorado, USA, and the 12th National Conference on Environmental Chemistry (NCEC) 2023 in Wuhan, China, which I had the privilege to attend.

I would like to thank my colleague, Karthik Shivakumar, with whom I collaborated closely on this project. His unwavering support and valuable advice proved instrumental, providing assistance whenever I encountered challenges in experiments or analyses. I would also like to thank Yuhao Li and Brendan Bishop. Yuhao Li helped me to conduct scanning electron microscope (SEM) analyses on my samples, while Brendan Bishop traveled from Regina to Saskatoon to assist me with X-ray absorption spectroscopy (XAS) measurements at the Canadian Light Source (CLS). Their contributions were invaluable to the success of this project.

Lastly, I express my sincere gratitude to my family, especially my parents, for funding me throughout the entire program and for their unwavering supports.

Table of Contents

List of Tables

List of Figures

1. INTROUDUCTION

1.1 Global demand of lithium

Lithium demand has increased dramatically over the past decade due to its widespread use in lithium-ion batteries (LIB) in electric vehicles (EVs), electronics, and large-scale grid storage applications.[1–3] In 2018, batteries consumed 37% of the overall lithium supply,[4] but the projection for 2023 indicates this proportion will rise dramatically to 80%.[5] Indeed, an estimated 134,000 tons of lithium was consumed globally in 2022, up 41% from 95,000 tons in 2021.[5] At the same time, the price of lithium has nearly tripled over the past three years[5], while global lithium production in 2022 climbed by 21% to about 130,000 tons from 107,000 tons in 2021.[5] The increase in global lithium demand surpasses the growth of global lithium production by a significant margin, a pattern which is anticipated to persist, indicating an imminent and substantial supply chain deficit. Furthermore, forecasts indicate that global lithium demand will exceed 2 million and 5 million tons by 2030 and 2050, respectively, while also suggesting that current established lithium resources could be depleted by 2080.[6]

The rapid increase in the demand for lithium has spurred the expansion of existing global lithium operations and ongoing initiatives to enhance production capacity. However, the limited availability of lithium resources has restricted production.[7,8] Moreover, Australia, Chile, China, and Argentina are the primary producers of lithium in 2022, contributing 46.9%, 30.0%, 14.6%, and 4.8% of global lithium production, respectively.[5] As a result, most other countries heavily rely on importing lithium from these producers. In response and to secure the lithium supply, there has been a global focus over the past decade toward developing alternative resources of lithium.[1]

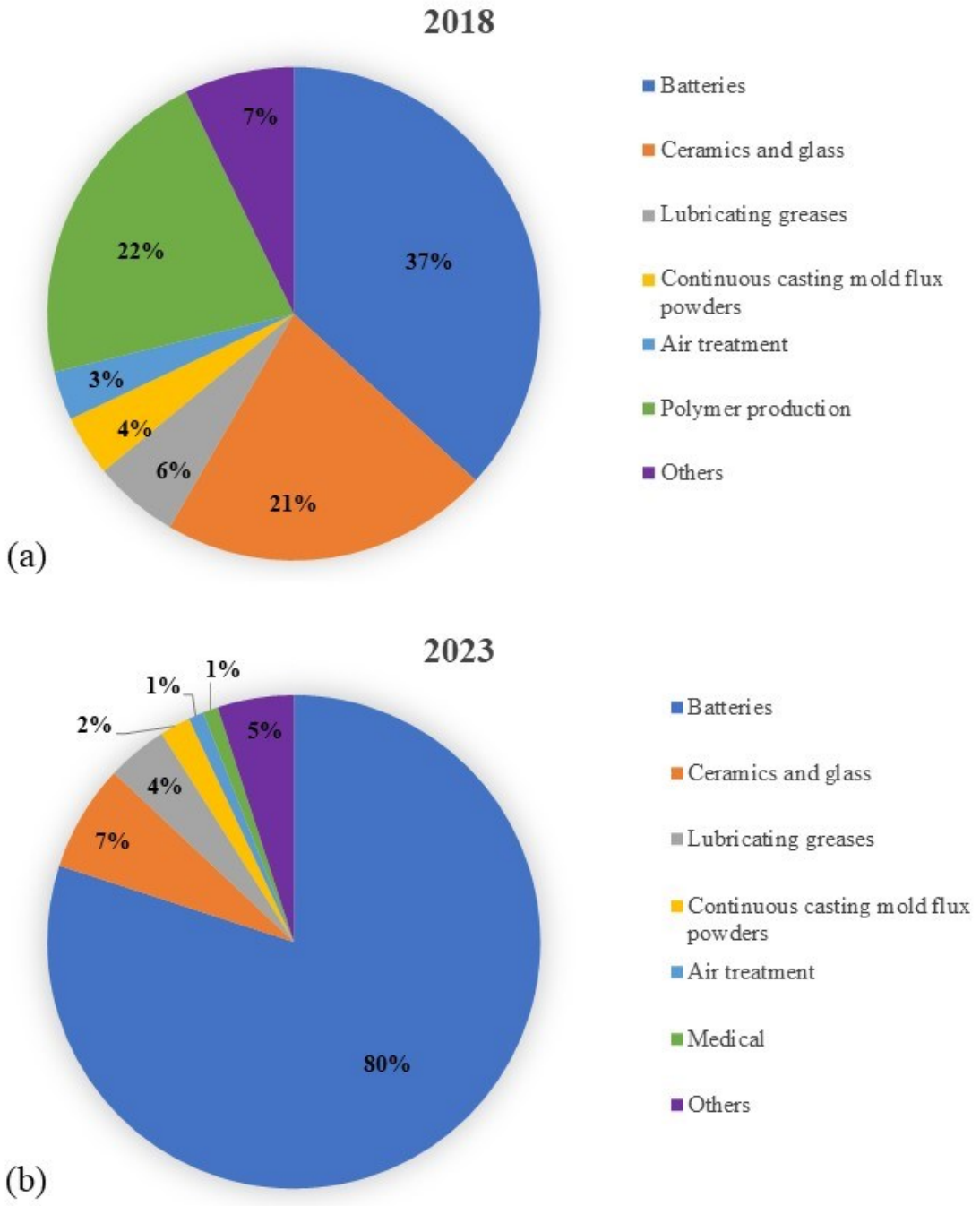

Figure 1: Distribution of global lithium end-usage in different industries in (a) 2018 and (b) 2023.[4,5]

1.2 Lithium Resources

Lithium stands out as one of the Earth's abundant elements, primarily found in mineral and brine deposits.[6,9–13] It is estimated that brine deposits make up approximately 62% of the total global lithium resource while mineral deposits comprise the remaining 38%.[13] The distribution of global lithium resources is illustrated in Figure 2. The largest portion (43.6%) of global lithium resources is situated in the Puna Plateau, an elevated Andean region known as the Lithium Triangle, formed by Argentina, Bolivia, and Chile.[10,11,13] Remarkably, the salars within this region host about 80% of the world's lithium brine resource.[10,11] Nearly equivalent proportions of the remaining lithium resource, around 25% each, are located in North America and Australasia.[13] Conversely, Europe and Africa hold relatively modest reserves of lithium, each accounting for less than 3%.[13]

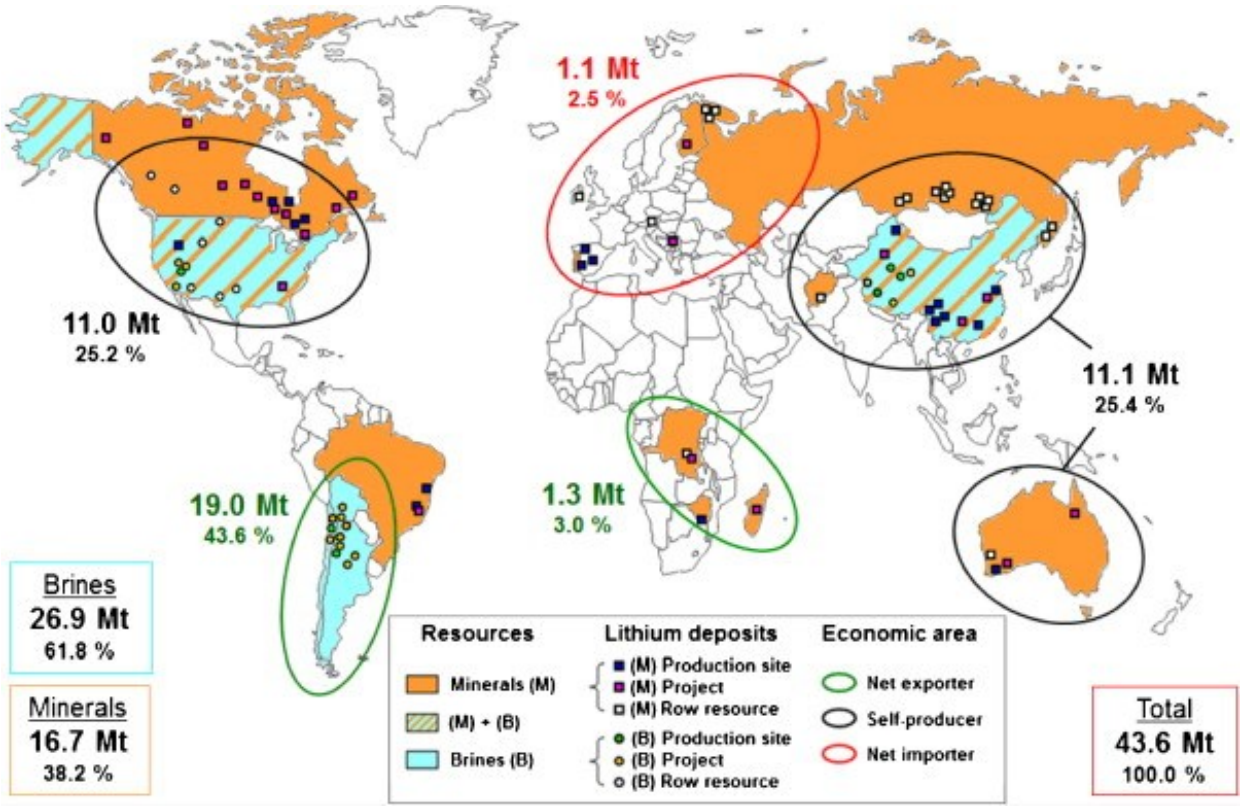

Figure 2: Map of global distribution for lithium resources. Adapted from Grosjean *et al.*[13]

1.2.1 Lithium in minerals

The most significant lithium deposits in minerals are found in granitic pegmatites,[2,6–8,11,14,15] which are holocrystalline intrusive igneous rocks that form during the final phase of magma crystallization.[16] Pegmatites often contain minerals that are rich in rare elements such as lithium, beryllium, tantalum, niobium, and rare-earth elements.[17] These elements are often incompatible with common minerals that crystallize earlier in the cooling process.[17] As the remaining molten magma becomes enriched in these rare elements at the late stage, it provides the necessary conditions for the formation of pegmatites.[17] Pegmatites are abundant and can be found all over the world,[2,7,11,14,15] with most located in Australia, China, the United States, and Canada.[8,13,15] Lithium concentrations in such rocks typically range between 1-4 wt%.[2,8,18] Lithium exists in pegmatites in various mineral forms, including aluminosilicates and phosphate minerals such as spodumene ($LiAlSi_2O_6$), lepidolite ($KLi_{1.5}Al_{1.5}[Si_3O_{10}][F,OH]_2$), petalite ($LiAlSi_4O_{10}$), zinnwaldite ($KLiFeAl[AlSi_3]O_{10}[OH,F]_2$) and amblygonite ($LiAl[PO_4][OH,F]$).[2,6–8,10,18] Among them, spodumene is the most important commercial ore mineral for large-scale lithium production due to its high lithium content (2.10-3.73 wt%) and abundance.[2,6,10,11,19] The traditional method of extracting lithium from spodumene using sulfuric acid is fairly efficient, achieving yields of 85-90%.[6] Petalite, which can contain 0.93-1.87 wt% lithium,[19] finds application in glass, glazes, and ceramics due to its high iron content and low thermal expansion features.[2,6,10] Lepidolite, containing 0.71-2.75 wt% lithium,[19] is no longer exploited in lithium mining due to its elevated fluorine content.[2,6,10]

1.2.2 Lithium in brine

Brines represent the world's largest lithium resources on land, and include continental brines, geothermal brines and oilfield brines.[6–8,11,14,15,18,20] These brines generally contain elevated

lithium concentrations, sometimes up to 4000 mg·L^{-1}, but with concurrent high concentrations of impurities (e.g. sodium, magnesium, calcium, chloride).[2,6,8,15] Notably, continental brines account for more than 50% of global lithium production,[15] and due to geological limitations, most (>80%) of them are in the Lithium Triangle comprised of Argentina, Bolivia, Chile, and in the Qinghai and Tibet provinces of China.[6,9,10] In contrast, many more countries have access to low lithium-bearing brines,[9] such as geothermal brines and oilfield brines,[3,6,9–12,14,21] which are considered to be a waste byproduct of geothermal energy and oil and gas exploitation.[1,14] Notionally, lithium concentrations in these low lithium-bearing brines must exceed a certain threshold (~75 mg·L^{-1}) to be economically extractable.[22] However, the presence of dissolved H_2S and organic compounds in the brines might necessitate a higher lithium concentration for the process to be economically viable.[1] In response to the lithium supply shortage, geothermal brines and oilfield brines are listed as potential resources for lithium production.[1,3,8–12,14,15,20] Therefore, there is a need for thorough exploration and investigation into the advancement of lithium recovery techniques for low lithium-bearing brines, specifically direct lithium extraction (DLE) technologies.[1,6,8,9,12–15,20]

1.3 Hydraulic fracturing flowback and produced water

Flowback and produced water is a waste byproduct of oil and gas production resulting from hydraulic fracturing activities.[1,20,21] In the initial stage of unconventional oil and gas development, fracturing fluids, which are comprised of water, sand and chemical additives, are injected into the targeted formation to create fractures.[1,21,23] These fractures establish permeable channels from the wellbore into the formation, then proppants in fracturing fluids hold these channels open, constructing permeable pathways for the flow of hydrocarbons.[24] During hydraulic fracturing process, water trapped within the formations mixes with the fracturing fluids and subsequently migrates to the surface.[1,23,25] This water that returns is referred to as FPW, and it constitutes a

complex mixture of dissolved inorganic species and organic compounds.[21,23,25–27] Lithium that initially resides in the formation water is also transported to the surface.

The chemistry of FPW is intimately tied to the geologic formation targeted for hydraulic fracturing. Typically, FPW is highly saline with total dissolved solids (TDS) ranging from 10,000 to 300,000 $mg \cdot L^{-1}$ depending on the formation.[1,26,28] Since lithium concentrations in such wastewater range from tens to hundreds of parts-per-million,[1,3] relatively low compared to salars, it is regarded as a low lithium bearing resource.[9] It is anticipated that the volume of FPW from oil and gas production will reach 499-3585 million m^3 in 2030 globally,[21] providing an excellent opportunity for untraditional lithium production.

1.4 FPW in western Canada

Eccles and Berhane reported lithium concentrations in formation brine in the Western Canadian Sedimentary Basin (WCSB) within Alberta, ranging up to approximately 140 $mg \cdot L^{-1}$.[27] Regions with elevated lithium concentrations occur in the Leduc formation of the Woodbend Group and the Swan Hills formation of the Beaverhill Lake Group in west-central Alberta.[23,27] It is estimated that around 515,000 tons of lithium carbonate equivalent (LCE) are potentially present in these formations.[23,27] The highest lithium concentrations were discovered in the Duvernay formation brine near Fox Creek, Alberta, where the average exceeds 75 $mg \cdot L^{-1}$.[23,27] Eccles and Berhane first hypothesized that the presence of lithium in sedimentary brines is a result of hydrothermal volcanic activity which brings lithium from the underlying igneous rock to the overlying sedimentary rocks.[27] Nonetheless, a recent study proposes an alternative theory that the lithium could have originated from ancient seawater.[23] This seawater might have evaporated and undergone concentration to create lithium-enriched brine.[23]

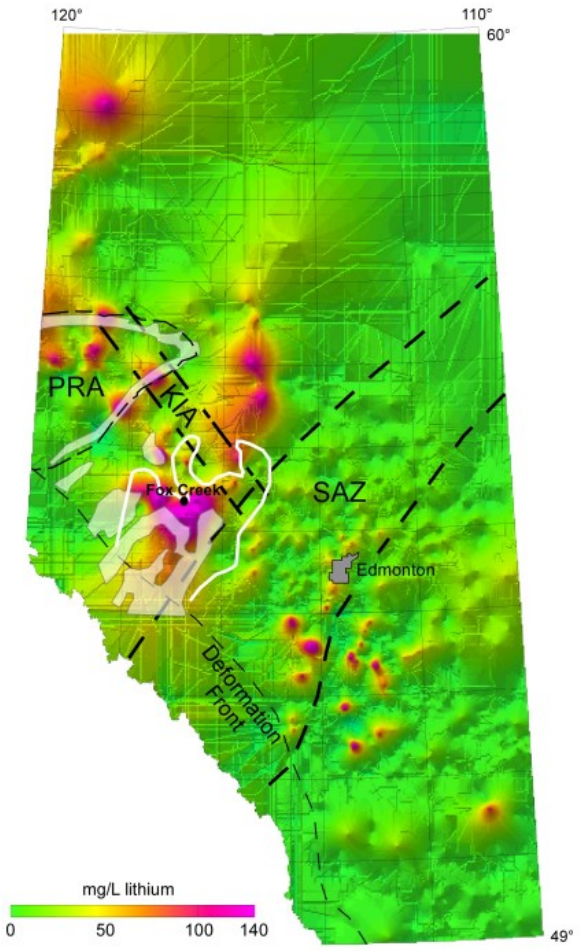

Figure 3: Map of lithium concentrations in formation waters in Alberta. Adapted from Eccles and Berhane.[27]

Hydraulic fracturing activities in the WCSB due to oil and gas exploration have generated vast volumes of FPW over the past decade,[23,25,27,29] establishing a continuous potential source of lithium. According to recent studies (Figure 4), the lithium concentrations in 106 FPW samples obtained from oil and gas producing wells in the Duvernay formation in the Fox Creek area fall within the range of 17-79 mg·L^{-1}, with an average of 45.1 mg·L^{-1}.[23,25] Furthermore, an ongoing investigation conducted by Geoscience BC and Geological Survey of Canada has sampled over 200 FPW collected from the Montney formation in the Dawson Creek region.[23,25] The results reveal that the lithium concentrations in these samples vary from 10 to 80 mg·L^{-1}, with an average

of 57.7 mg·L^{-1}.[23,25] Meanwhile, the average mass ratios of Mg^{2+}/Li^{+} are 20 and 31 for the samples from Duvernay and Montney formation, respectively.[23] Despite the low concentrations of lithium in FPW in WCSB, the volumes of fluid present along with the existing infrastructure could potentially turn lithium extraction from FPW in WCSB into a profitable venture.

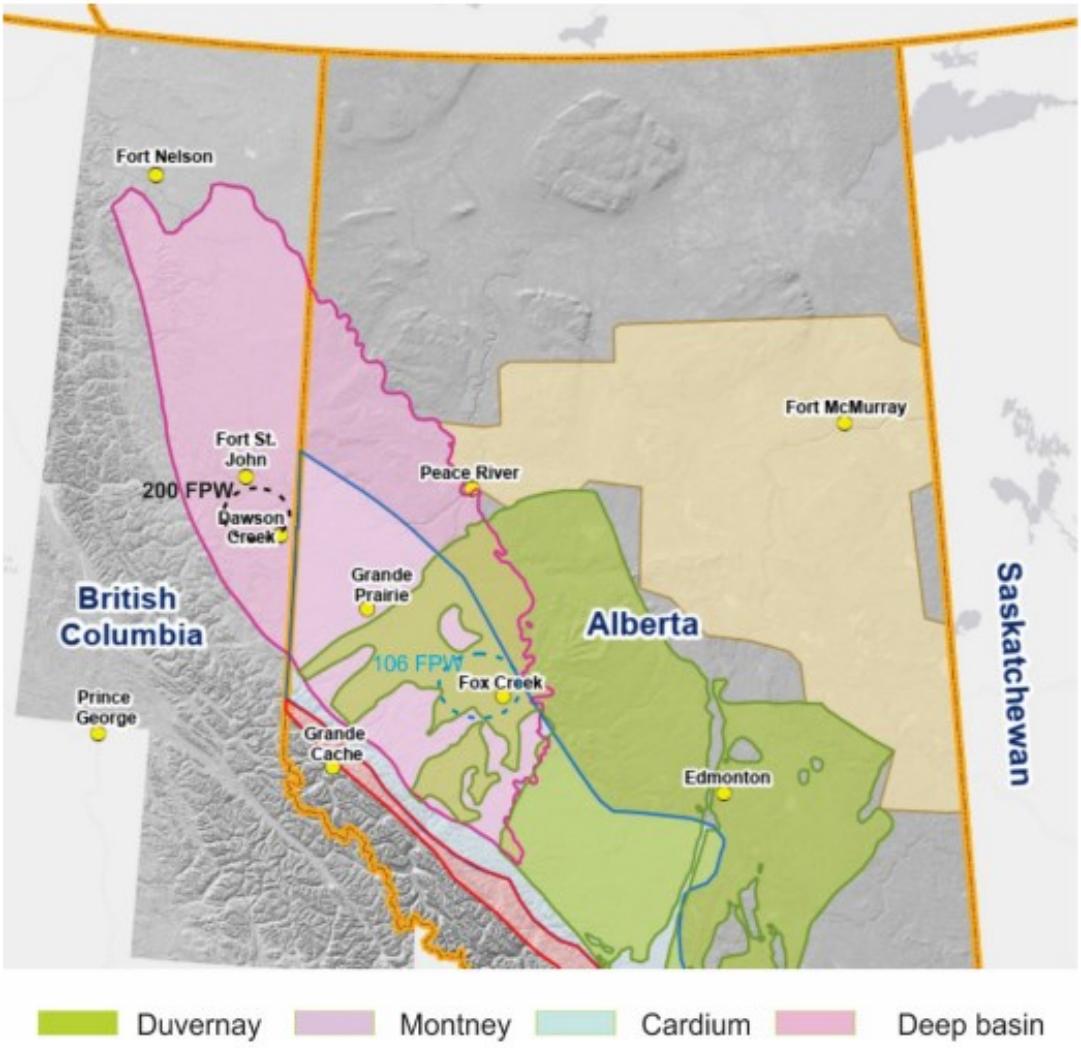

Figure 4: Locations of flowback and produced water (FPW) samples from the Duvernay (106) and Montney (200) formations. Adapted from Leece and Jiang.[23]

1.5 Traditional lithium extraction from brine

Solar evaporation combined with precipitation has been the primary method to recover lithium from brines for the past several decades.[6,9] It is the only method applied in the industrial large-scale production of lithium from brines due to its simplicity and low cost.[3,10] This method is geographically limited to regions with long summer days, moderate wind, little rain, and low humidity, which promote water evaporation.[3,6] Due to geographic limitations, there are only eight large-scale commercial facilities currently employing this technology for lithium production in the world,[9,11] most of them are located in the Lithium Triangle, characterized by high elevations that promote evaporation.[2,8,10]

To extract lithium in this way, lithium-containing brine is pumped from underground reservoirs into large evaporation ponds, followed by several months of solar evaporation until lithium chloride (LiCl) concentrations reach ~6000 mg·L^{-1}.[6,10] During this long process, 90% of water is evaporated.[9] Then the remaining concentrated brines are transferred to recovery ponds and treated with lime ($Ca(OH)_2$) to remove Mg^{2+} and sulfate (SO_4^{2-}) as magnesium hydroxide ($Mg(OH)_2$) and calcium sulfate ($CaSO_4$), respectively.[6] Subsequently, sodium carbonate (Na_2CO_3) is added to remove Ca^{2+} as calcium carbonate ($CaCO_3$).[6,9,12] Meanwhile, lithium carbonate (Li_2CO_3) starts to precipitate after continuously adding $CaCO_3$.[6,9,12] Finally, the initial Li_2CO_3 product must go through repeated dissolution and re-precipitation processes until it reaches battery-grade purity (>99.5 wt%). [6,10,12]

Despite the low cost of traditional lithium production from brines, the evaporation process is time-consuming, water-wasting and land-intensive.[14] Depending on the climate (e.g., sunlight, humidity, and rainfall), the pace of the entire lithium production process tends to be slow, requiring 12-24 months.[1,6] Significant amounts of water, ranging from 100 to 800 m^3 per ton of Li_2CO_3, are

lost during the process.[9] On average, a salar generating 18,000 metric tons annually will result in approximately 2×10^7 tons of waste, requiring a land area of ~10 km^2.[6,11] More importantly, this traditional process only achieves ~50% of lithium recovery rate.[30] Additionally, the leaching of dissolved salts (e.g., Na_2CO_3 and Li_2CO_3) into the surrounding areas contaminates soils and freshwater supplies, raising environmental and social concerns.[6] It is worth noting that the amount of Mg^{2+} in brines plays an important role in the precipitation process.[6,12,31] Initially, elevated levels of Mg^{2+} decelerate the evaporation process and inhibit the formation of LiCl.[6,31] Moreover, excessive Mg^{2+} leads to overconsumption of precipitants ($Ca(OH)_2$ and Na_2CO_3, resulting in a higher processing cost and a loss of lithium.[6,12,31] For these reasons, brines with Mg^{2+}/Li^+ mass ratios exceeding 10 are not economically feasible using the evaporation and precipitation method.[6]

The economic feasibility of lithium extraction using this traditional evaporation method from low-lithium bearing brines depends on four factors: (1) local climate; (2) Li^+ concentration in brine; (3) mass ratio of Mg^{2+} /Li^+ in brine; (4) the production cycle.[6] Due to the long and cold winters, low concentrations of lithium relative to salars, and high mass ratios of Mg^{2+}/Li^+, this traditional lithium extraction method is not suitable for lithium recovery from FPW in Canada.

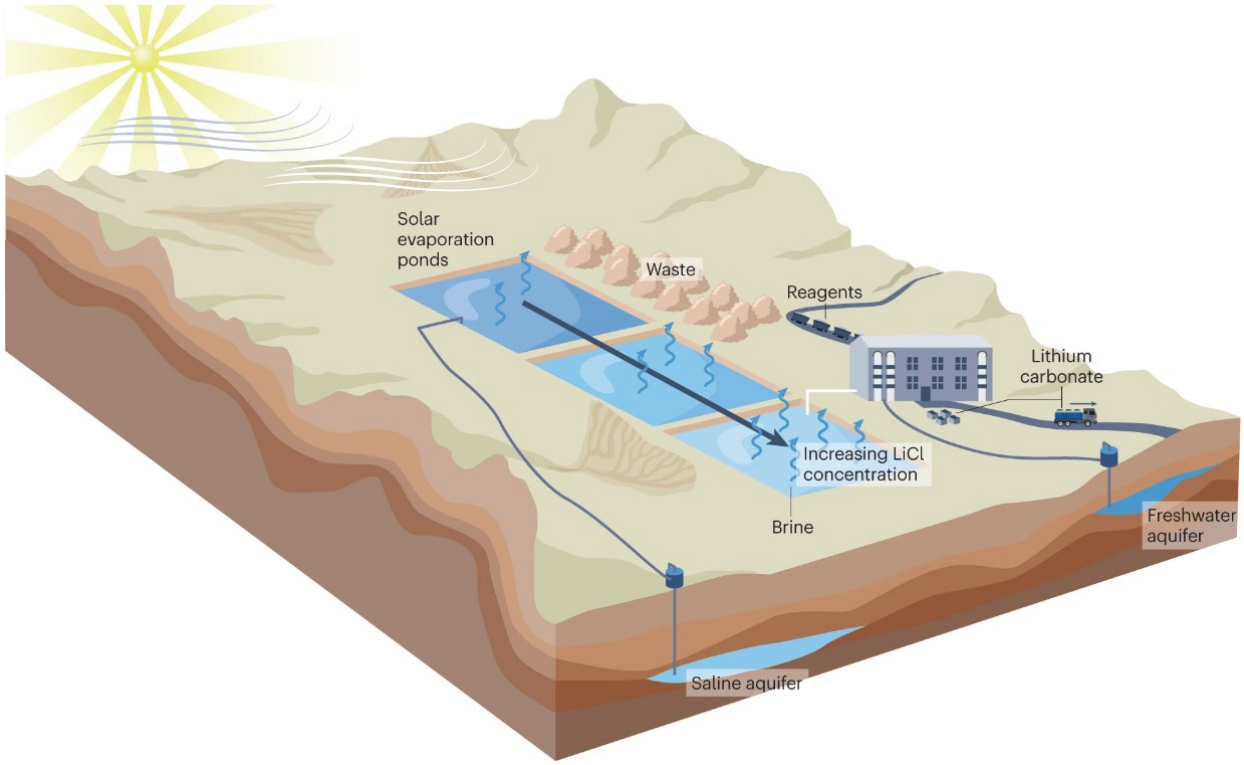

Figure 5: Schematic representation of evaporitic technology. Adapted from Vera *et al.*[9]

1.6 Direct lithium extraction (DLE)

DLE technologies are designed to separate lithium from unconventional aqueous resources while overcoming the environmental and economic constraints of conventional evaporative method.[9] Theoretically, DLE eliminates the need for open air evaporation ponds, reducing environmental footprint.[9] Studies have documented that electrochemistry, solvent extraction, membrane, and adsorption are the common DLE methods for recovering lithium from brine.[1,3,6,7,10,12,14,20]

1.6.1 Electrochemistry

The electrochemical recovery of lithium is based on the principle of a lithium-ion battery, which uses a redox couple (e.g., $LiFePO_4$/ $FePO_4$, $LiMn_2O_4$/λ-MnO_2) as a working electrode to

capture Li^+ from solution, driven by changes in an electric field.[6,10,12,32–35] In the extraction (discharging) step, Li^+ moves toward and intercalates into the cathode due to redox reactions ($2Mn^{3+} \longrightarrow Mn^{2+} + Mn^{4+}$).[10,33] By reversing the direction of electric current flow (charging step), Li^+ can be released from the electrode into a recovery solution.[10,33] However, this electrochemical process must operate under a continuous electric current flow, resulting in high energy consumption.[6] Furthermore, the presence of high concentrations of other cations, such as Mg^{2+}, K^+, and Na^+, in brines can impact Li^+ recovery efficiency and selectivity, as these cations also move toward the cathode during the discharging step.[1,6] Electrochemistry is not suitable for lithium recovery from FPW due to the presence of high concentrations of other cations in FPW, which significantly affect Li^+ recovery efficiency and selectivity.

1.6.2 Solvent extraction

Solvent extraction of lithium, also known as liquid-liquid extraction (LLE), is based on the relative solubilities of Li^+ in two immiscible liquid phases.[6,10,12] When the Li brine (the aqueous phase) is mixed with the organic solvent (the organic phase), Li^+ is transferred to the organic liquid phase.[6,10,12] Subsequently, the Li^+ loaded organic phase is added to a recovery solution (an acid) to release Li^+.[6,10,12] However, this process produces large volumes of acid wastewater and potentially toxic organic waste.[6,12] Additionally, the corrosive additive used in solvent extraction can cause severe damage to the environment in the case of a release, and it can also damage the process equipment.[1,6,36] More importantly, most solvents with the ability to separate lithium from divalent cations also show a strong affinity for sodium.[37] Consequently, implementing this method may necessitate pre-treatment steps to eliminate sodium, which is generally more abundant than lithium in brines.[37] Moreover, this method must be combined with other extraction techniques because of

its limited selectivity toward lithium.[12] For these reasons, solvent extraction method is not considered to be suitable for lithium recovery from FPW.

1.6.3 Membranes

Membrane process, also known as reverse osmosis, is an effective method to separate substances in brines due to the selective permeability of materials.[6,10,14,31] Brines pass through the membrane driven by a pressure, concentration, or electric potential difference.[10,12,14,31] A membrane can have selectively to Li^+ because it allows permeation of small monovalent ions, such as Li^+, and blocks large divalent ions.[6,14,31] However, membranes typically exhibit a low lithium recovery (<80%) and may require an additional step to concentrate lithium from filtrates,[3] which results in an increase in operation cost. Further, they lose efficiency when fouling occurs.[3,12] This method is not suitable for lithium recovery from FPW with high concentrations of monovalent ions.

1.6.4 Selective adsorption

Selective adsorption is regarded as one of the most suitable DLE technologies for extracting lithium from low lithium-bearing brines such as FPW due to its high selective to lithium, economical and eco-friendly features.[1,3] Lithium adsorbent materials, also known as lithium ion-sieves (LIS), predominantly refers to aluminum hydroxide, lithium manganese oxides (LMOs) and lithium titanium oxides (LTOs).[1,3,6,10,14,20,31,38] LIS are inorganic compounds in which the target (lithium) ions are initially incorporated through redox or ion-exchange reactions and subsequently removed from the structure using an eluent.[3,6,10,31] The mechanisms behind their adsorption involve physisorption facilitated by electrostatic forces and chemical adsorption driven by ion exchange.[6,10] LIS exhibit a high degree of selectivity for lithium due to the similarity in size between the ion radii of lithium ions and the adsorption sites of the adsorbents.[1,3,6,10,14]

Aluminum hydroxide adsorbents with the general chemical formula $[LiAl_2(OH)_6]^+Cl^-\cdot nH_2O$,[3] referred to as lithium-aluminum-layered double hydroxide chloride (LiAl-LDH),[31] are formed by the insertion of lithium salts (i.e. LiCl) into $Al(OH)_3$.[3,12,31] Kotsupalo et al. employed LiAl-LDH adsorbents with structural defects to recover lithium from a brine having a high Mg^{2+}/Li^+ ratio.[39] The adsorbent exhibited a high selectivity toward lithium, but the uptake was below 8.0 $mg\cdot g^{-1}$,[39] which was relatively low compared to other DLE materials. Jiang et al. studied the kinetics of lithium adsorption on LiAl-LDH adsorbents; lithium uptake reached equilibrium in 10 hours at an uptake of 3.0 $mg\cdot g^{-1}$.[40] Zhong et al. also synthesized LiAl-LDH adsorbents using a coprecipitation method and reported a maximum lithium uptake of 7.3 $mg\cdot g^{-1}$ when recovering lithium from a salar brine.[41] Degradation of LiAl-LDH to gibbsite ($Al(OH)_3$) occurs when LiCl is excessively removed during delithiation, damaging the reusability of the adsorbent.[3] Despite this limitation, LiAl-LDH adsorbents are currently the only materials utilized in industrial applications, but their low adsorption capacities and slow adsorption rates present challenges in commercialization.[3,10,31]

In contrast to aluminum hydroxide adsorbents, LMOs and LTOs have attracted greater interest in academic research and industrial applications, owing to their high selectivity toward lithium, excellent lithium absorption capacity, rapid kinetics of Li uptake and release, and ease of reuse.[1,3,10,14,36] Common LMO-type LIS precursors are $LiMn_2O_4$, $Li_{1.33}Mn_{1.67}O_4$ and $Li_{1.6}Mn_{1.6}O_4$, and common LTO-type LIS precursors are Li_2TiO_3 and $Li_4Ti_5O_{12}$.[3,10,31,32] Theoretically, the lithium uptakes of $Li_{1.6}Mn_{1.6}O_4$ and Li_2TiO_3 can reach 73 $mg\cdot g^{-1}$ and 140 $mg\cdot g^{-1}$, respectively.[3] The lithium recovery process utilizing LMOs or LTOs follows a three-step pH-dependent ion exchange process, which can be referred to as the "LIS effect", depicted in Figure 6.[42] Following synthesis and before use in recovering lithium from a fluid, the LIS is exposed to an acidic solution to remove the

lithium in ion exchange sites and replace it with protons. Subsequently, it is immersed in a lithium-bearing brine adjusted to mildly alkaline conditions to adsorb lithium. LIS only targets Li^+ from the coexistence of other major ions (Mg^{2+}, Ca^{2+}, Na^+, K^+) due to the small ionic radius of Li^+.[43] Despite the close ionic radii between Mg^{2+} (0.072 nm) and Li^+ (0.069 nm), LIS materials are not selective to Mg^{2+} because a higher dehydration energy Mg^{2+} is required for them to enter the LIS.[43] Finally, the LIS is regenerated by releasing the inserted lithium from the adsorbent through an acid desorption reaction, concentrating the lithium in a small amount of acid.

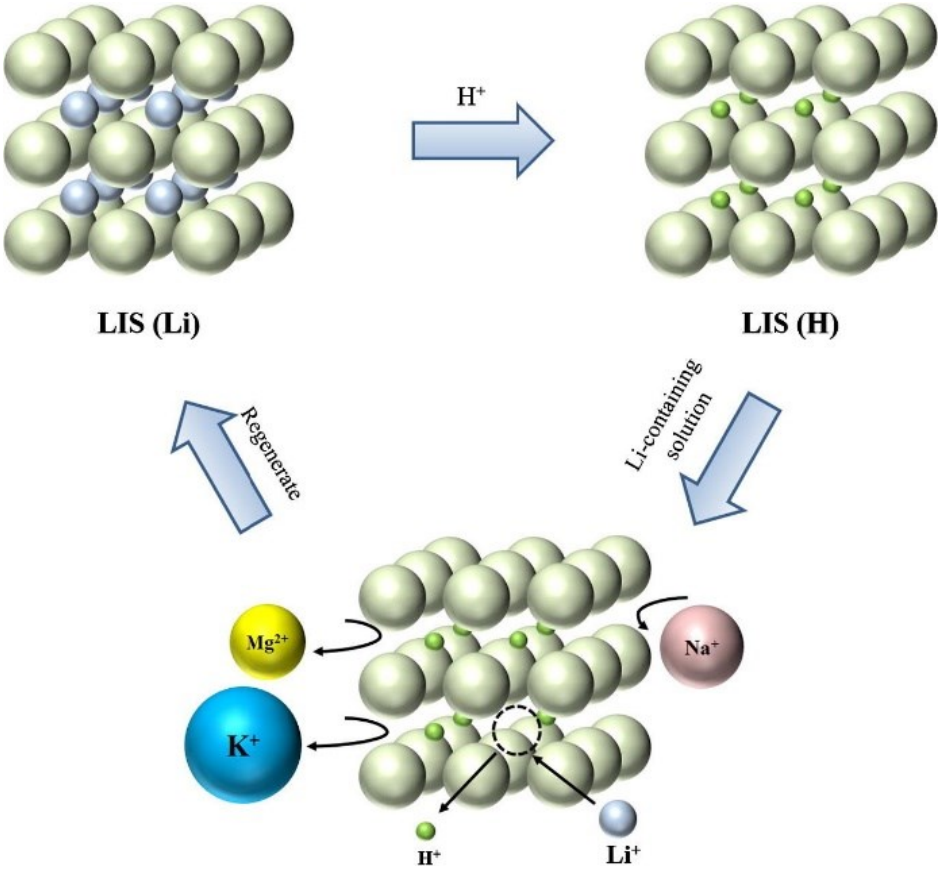

Figure 6: Schematic of the lithium recovery using LMO or LTO ion sieves and ion sieves effect. Adapted from Xu *et al.*[42]

1.7 Spinel lithium manganese oxide adsorbent

Spinel lithium manganese oxides have the general formula (Li)[Li_xMn_{2-x}]O_4, where () represents the tetrahedral sites (8a) and [ ] represents the octahedral sites (16d) in the cubic closed-packed oxygen framework (32e).[1,3,44] Extant studies have demonstrated that there are two adsorption mechanisms for spinel lithium manganese oxides: a redox mechanism and an ion exchange mechanism, as expressed by *equations* 1a and 1b, and 2, respectively:[1,3,44]

$$4(Li)[Mn^{3+}Mn^{4+}]O_4 + 8H^+ \rightarrow 3(\,)[Mn_2^{4+}]O_4 + 4Li^+ + 2Mn^{2+} + 4H_2O \qquad (equation\ 1a)$$

$$(\,)[Mn_2^{4+}]O_4 + nLiOH \rightarrow (Li_{n\,1-n})[Mn_n^{3+}Mn_{2-n}^{4+}]O_4 + \frac{n}{2}H_2O + \frac{n}{2}O_2 \qquad (equation\ 1b)$$

$$Li_xMn_yO_4 + xH^+ \leftrightarrow H_xMn_yO_4 + xLi^+ \qquad (equation\ 2)$$

Manganese in the LMO exists in both trivalent manganese (Mn^{3+}) and tetravalent manganese (Mn^{4+}) forms.[3,44] The LMO precursors, e.g., $LiMn_2O_4$, which contain only Mn^{3+} follow the redox mechanism; whereas those that contain exclusively Mn^{4+} (i.e. $Li_{1.33}Mn_{1.67}O_4$ and $Li_{1.6}Mn_{1.6}O_4$) follow an ion-exchange mechanism.[1,3,42,44] For a redox-type LMO that contains trivalent manganese in the bulk material, reductive dissolution of Mn^{3+} to divalent manganese (Mn^{2+}) occurs during lithium desorption, resulting in Mn^{2+} dissolution in the acid, as indicated in *equation* 1a.[1,44] The dissolution of Mn^{2+} further induces structural distortion, leading to a reduction in lithium uptake of the adsorbent during recycling. Consequently, this behavior shortens the adsorbent's lifetime.[3,44] Therefore, a redox-type LMO is not suitable for DLE applications. Ideally, an adsorbent should have the capacity for being reused at least a hundred times to attain economic feasibility in commercial lithium production from low lithium-bearing brines. Additionally, theoretical Li uptake of ion-exchange type LMO (60 mg·g^{-1} for $Li_{1.33}Mn_{1.67}O_4$ and 73 mg·g^{-1} for $Li_{1.6}Mn_{1.6}O_4$) is higher than that of redox-type LMO (40 mg·g^{-1} for $LiMn_2O_4$).[36] LMOs also exhibit

faster Li uptake rates compared to LTOs.[3] For these reasons, ion-exchange type $Li_{1.33}Mn_{1.67}O_4$ and $Li_{1.6}Mn_{1.6}O_4$ have gained interests in the advancement of DLE applications, which is also the motivation of why $Li_{1.6}Mn_{1.6}O_4$ is being investigated in this study.

1.8 Previous work

In previous research, Seip et al. synthesized an ion exchange type of LMO adsorbent ($Li_{1.6}Mn_{1.6}O_4$) and tested it in an FPW containing a low lithium concentration (43 $mg \cdot L^{-1}$).[1] The absorbent exhibited a high selectivity for Li in the brine with lithium absorption of 18 $mg \cdot g^{-1}$; however, a considerable amount of Mn was dissolved and lost in the acid desorption step to recover Li.[1] Importantly, Seip et al. also demonstrated that H_2S and dissolved organic compounds present in the FPW can reduce Mn^{4+} to Mn^{3+} in the adsorbent during lithium adsorption, further leading to Mn^{2+} dissolution in acid during desorption.[1] Many studies have demonstrated that coating and doping can effectively inhibit Mn dissolution, thus improving the stability of LMO.[3] Dopants, such as Na^+, Mg^{2+}, Co^{2+}, Al^{3+}, Fe^{3+}, and Ti^{4+} substitute for Mn^{3+} in 16d sites, forming stronger bonds with oxygen in the lattice.[45–56] Qian et al. synthesized a number of doped $Li_{1.6}Mn_{1.6}O_4$ with Na^+, Co^{2+}, Fe^{3+} and Al^{3+} by hydrothermal methods; the doped adsorbents exhibited higher Li^+ uptakes in salt lake brines and lower Mn dissolutions in acid.[46–48] A series of Ti-doped lithium manganese oxides $Li_{1.33}Ti_xMn_{1.67-x}O_4$ were synthesized by Ryu et al. using a solid-state reaction, and the Mn^{2+} dissolution was reduced from 3.5% to 2.1%.[50] More interestingly, the Li^+ uptake in seawater decreased with increased Ti^{4+} doping, while Mn dissolution increased with higher calcination temperatures.[50] Chitrakar et al. employed iron-doped lithium manganese oxides, $Li_{1.33}Fe_xMn_{1.67-x}O_4$, for the recovery of Li in $NaHCO_3$/NaOH-treated salar brine and revealed a significant enhancement in Li^+ uptake in treated brine compared to an untreated one.[53]

While the utilization of cation-doped LMOs has been explored in various aqueous lithium resources, to the best of my knowledge, no study has been conducted on cation-doped LMOs for lithium recovery from FPW. Furthermore, the effects of introducing foreign cations through doping into the LMO structure on lithium adsorption and desorption remains uncertain.

1.9 Research purpose and objective

Manganese dissolution of LMOs poses a significant barrier to the commercialization of this DLE technology.[1] Being able to recycle the adsorbent at least a hundred times is essential for achieving economic feasibility in commercial lithium production. Therefore, in order to address the issue of Mn dissolution and improve the stability of LMOs, a pristine LMO was doped with magnesium in this study. Magnesium was selected as the dopant due to its ubiquity, low cost, and ability to be directly obtained from FPW.

The objectives of this research are as follows:

1. To prepare a series of magnesium-doped lithium manganese oxides (LMMO-x, x = 0.1, 0.2, 0.3, 0.4) and pristine LMO adsorbents, and to perform lithium recovery experiments from FPW to determine the effects of Mg doping on lithium adsorption performance. Lithium adsorption was modelled using three common kinetics models: the pseudo-first-order (PFO) model, pseudo-second-order (PSO) model and intraparticle diffusion model.
2. To perform lithium recovery experiments from both FPW and a synthetic brine to compare the performance of the adsorbents in terms of lithium uptake and manganese dissolution between the two types of brines, thus determine the effects of Mg doping on the ability of the adsorbents to resist Mn reduction due to complex dissolved organic compounds in the field collected FPW.

3. To perform lithium recovery experiments from field collected FPW and regenerate the adsorbents up to five cycles of adsorption and desorption to compare the stabilities of the adsorbents. Stability was determined from the lithium uptake and manganese dissolution at the fifth cycle.
4. To perform a series of chemical and physical characterizations on the adsorbents, aiming at elucidating structural transformations of the adsorbents as magnesium ions are introduced into the structure and during lithium adsorption/desorption cycles.

Overall, this study aims to fix the issue of Mn dissolution and improve the stability of LMO by magnesium doping in order for this technology to be commercially viable. It also provides valuable insights into the effects of magnesium doping on LMOs in terms of lithium uptake, manganese dissolution and structural transformation, allowing for future development of optimized DLE adsorbents associated with lithium recovery from natural FPW.

2. MATERIAL AND METHODS

2.1 Materials

Lithium hydroxide monohydrate ($LiOH\cdot H_2O$, 98%), manganese chloride tetrahydrate ($MnCl_2\cdot 4H_2O$, >99%), magnesium nitrate hexahydrate ($Mg(NO_3)_2\cdot 6H_2O$, >99%), hydrogen peroxide (H_2O_2, 30% in water), sulfuric acid (H_2SO_4, 98%), sodium hydroxide (NaOH, >99%), ammonium oxalate monohydrate ($(NH_4)_2C_2O_4\cdot H_2O$, >99%), potassium permanganate ($KMnO_4$, >99%), sodium chloride (NaCl, >99%), sodium bicarbonate ($NaHCO_3$, 99.5%), sodium bromide (NaBr, 98%), lithium chloride (LiCl, >99%), potassium chloride (KCl, 99%), magnesium chloride hexahydrate ($MgCl_2\cdot 6H_2O$, 99%), ferrous sulfate heptahydrate ($FeSO_4\cdot 7H_2O$, >99%) and manganese dioxide (MnO_2, 98%) were purchased from Fisher Scientific, Canada. Lithium manganese dioxide ($LiMnO_2$, >99%) and lithium manganese (Mn^{3+}, Mn^{4+}) oxide ($LiMn_2O_4$, >99%) were purchased from Sigma Aldrich, Canada. All chemicals were of analytical-reagent grade or better and were used without further purification. All solutions were prepared using ultra-pure water with a resistivity of 18.2 MΩ cm at 25°C.

The FPW sample used in this study was collected from a hydraulically fractured well (Well ID: 103/01-12-063-21W5) located near Fox Creek, Alberta, Canada on November 1st, 2016. The well was horizontally drilled into the Duvernay formation at a vertical depth of over 3 km. The FPW sample underwent analysis for the concentrations of major elements using an Agilent 8800 Triple Quadrupole Inductively Coupled Plasma-Mass Spectrometry (ICP-MS/MS), while the concentrations of major anions (Cl^- and SO_4^{2-}) and the concentration of total organic carbon (TOC) were previously documented by Zhong *et al*.[57] Table 1 shows the major chemical constituents and their concentrations in the FPW sample.

Table 1: Major chemical constituents of the FPW sample used in this study.

Parameter	Field Collected FPW
pH	3.62
TDS	220,000 mg·L^{-1}
TOC	283 mg·L^{-1}
Li^+	70 mg·L^{-1}
Mg^{2+}	1,225 mg·L^{-1}
Na^+	51,346 mg·L^{-1}
K^+	2,000 mg·L^{-1}
Ca^{2+}	11,189 mg·L^{-1}
Sr^{2+}	985 mg·L^{-1}
Fe^{2+}	140 mg·L^{-1}
Cl-	119,780 mg·L^{-1}
Br^-	235 mg·L^{-1}
SO_4^{2-}	59 mg·L^{-1}

2.2 Preparation of LMO and LMMOs

Pristine LMO was prepared using a co-precipitation method following Seip *et al.*[1] To do so, solid $MnCl_2 \cdot 4H_2O$ and $LiOH \cdot H_2O$ were dissolved in deionized water to make 0.375 M $MnCl_2$ and 3.0 M LiOH solutions, respectively. 3.0 M LiOH was added dropwise to 0.375 M $MnCl_2$ solution at a Li:Mn molar ratio of 3:1 while the solution was agitated at 300 rpm using a magnetic stir bar at room temperature, to form a black slurry of $Mn(OH)_2$. Then, 30% H_2O_2 was added dropwise to the mixed solution at a H_2O_2:Mn molar ratio of 10:1 to oxidize manganese. After stirring for 1 hour, the resulting solution was dried at 90 °C for 12 hours. The dry sample was further ground to a fine powder and calcinated at 450 °C for 4 hours to obtain the LMO. The magnesium doped precursors LMMO-x were subsequently synthesized by calcinating a mixture of LMO and a stoichiometric amount of $Mg(NO_3)_2.6H_2O$ solid. A total of 100 mg of each precursor

was added to 10 mL of 0.50 M H_2SO_4 and stirred at 40 rpm for 24 hours to obtain the protonated adsorbents (HMO and HMMO-x).

2.3 Adsorbent characterization

2.3.1 Physical analysis

The microstructure and morphology of the adsorbents were investigated by scanning electron microscopy (SEM) and transmission electron microscopy (TEM). Thermogravimetric analysis (TGA) was conducted using a TA Instruments TGA Q50. Specifically, about 15.0 mg of the adsorbents, precisely weighed, were heated up from 30 °C to 1000 °C at a rate of 10 °C·min^{-1} under a nitrogen gas environment.

X-ray absorption spectroscopy (XAS) analyses were performed at Hard X-ray Micro-Analysis (HXMA) beamline at the Canadian Light Source (CLS). The calcined, 1st protonated, 1st Li-reinserted, 2nd protonated and 5th protonated adsorbents were measured over the first 4 cycles of LMO cycle testing. The samples were prepared by mixing 10 mg of the above samples with 150 mg of boron nitride (BN) powder with a mortar and pestle. The mixture was pressed to a pellet using a hydraulic press to make a pellet, and then placed on a sample holder covered by a piece of Kapton® tape. The incident energy was selected using a Si (311) double crystal monochromator pair with an intrinsic energy resolution of 0.3 eV. X-ray absorption near edge structure (XANES) spectra were recorded from *ca.* 200 eV before the Mn K-edge (6539 eV) to 50 eV after the edge at a step size of 0.50 eV, whereas extended X-ray absorption fine structure (EXAFS) spectra were obtained with a finer 0.05 eV step size, covering energies of up to 1600 eV beyond the edge. XANES and EXAFS data were measured in transmission mode, and analyzed using the software packages ATHENA and ARTEMIS, respectively. The manganese average oxidation state (Z_{Mn}) values from XANES spectra were obtained through linear combination modelling in ATHENA,

with $LiMnO_2$, $LiMn_2O_4$, and MnO_2 serving as reference materials for Z_{Mn} values of 3.0, 3.5, and 4.0, respectively.

2.3.2 Chemical analysis

The chemical formulae and Z_{Mn} of each adsorbent were determined using the standard oxalic acid method.[1,58] 90 mg of each adsorbent was completely digested in 6 mL of 4.0 M H_2SO_4 and 12.5 mL of 0.10 M $(NH_4)_2C_2O_4$ in a water bath at 70 °C. 0.5 mL of the solution was then taken and analyzed using ICP-MS/MS to determine Li, Mn, and Mg concentrations in the adsorbents. The remaining solution was titrated with 0.01 M $KMnO_4$ to a faint pink endpoint to determine the moles of electrons transferred between oxalate and Mn. Subsequently, Z_{Mn} was estimated from the moles of transferred electrons and the total moles of Mn in the adsorbent. A general chemical formula of the form $Li_nMg_xMn_yO_4$ for the LMMO-x adsorbents was obtained from the ratios of Li/Mn, Mg/Mn, and Z_{Mn} using the following *equations*:[44]

$$\frac{8}{Li/(Mn+Mg)+Z_{Mn}} = x + y \qquad (equation\ 3)$$

$$\frac{Mg}{Mn} = \frac{x}{y} \qquad (equation\ 4)$$

$$\frac{n}{Li/(Mn+Mg)} = x + y \qquad (equation\ 5)$$

2.4 Adsorption and desorption experiments

Li^+ adsorption experiments were conducted using two brines: field collected FPW and synthetic brine. Seip *et al.* determined the optimum pH for Li^+ adsorption to be 8,[1] and we adjusted the pH of the brines accordingly by adding small aliquots of 0.1 M NaOH. The protonated adsorbents were added to both brines at a dosage of 2.0 g L^{-1}, then stirred at 40 rpm for 2 hours,

followed by centrifugation at a force of 6198 g for 5 minutes. The supernatant of the mixture was collected and analyzed by ICP-MS/MS to measure the remaining Li^+ concentration in the brine. Li^+ uptake was then calculated using a mass balance shown in *equation* 6:[59,60]

$$q_e = \frac{\rho_i - \rho_e}{M} \times V \qquad (equation\ 6)$$

Where q_e is the Li^+ uptake ($mg \cdot g^{-1}$), ρ_i and ρ_e are the initial and final Li^+ concentrations ($mg \cdot L^{-1}$), respectively, V is the volume of FPW or synthetic brine (L), and M is the mass of the adsorbent (mg).

The lithium-reinserted adsorbents were washed twice with deionized water and dried at room temperature. The dried adsorbents were then added at a dosage of 6.0 $mg \cdot g^{-1}$ to two different concentrations (0.1 M and 0.5 M) of H_2SO_4 to extract Li^+ with constant stirring at 40 rpm for 30 minutes, followed by centrifugation at a force of 6198 g for 5 minutes. The lithium concentrate resulting from the acid desorption step was also analyzed by ICP-MS/MS to calculate Li^+ desorption efficiency and Mn^{2+} dissolution. Li^+ desorption efficiency and Mn^{2+} dissolution were calculated using *equations* 7 and 8, respectively:[61]

$$\text{Li}^+ \text{ desorption efficiency } (\%) = \frac{amount\ of\ \text{Li}^+\ desorbed}{amount\ of\ \text{Li}^+\ adsorbed} \times 100\% \qquad (equation\ 7)$$

$$\text{Mn}^{2+} \text{ dissolution } (\%) = \frac{\rho(\text{Mn}^{2+})V}{Mw(\text{Mn})} \times 100\% \qquad (equation\ 8)$$

Where $\rho(\text{Mn}^{2+})$ is the concentration of Mn^{2+} in the desorption acid ($mg \cdot L^{-1}$), V is the volume of the acid (L), and $w(\text{Mn})$ is the mass fraction of Mn in the adsorbent.

2.4.1 Li^+ Selectivity

The presence of high concentrations of co-existing ions in FPW can have a significant effect on the adsorption of Li^+.[3] To investigate this effect, the selectivity of the adsorbents was examined by adding 50.0 mg of adsorbent to 25 mL of the pH-adjusted FPW followed by stirring for 24 hours. Samples of the FPW were taken before and after adsorption and analyzed using ICP-MS/MS. The initial and final concentrations of major cation ions were compared, and the partitioning coefficients (K_d) and separation factors (α_N^{Li}) were calculated using *equations* 9 and 10, respectively:[60,61]

$$K_d = \frac{\rho_i - \rho_e}{\rho_e} \times \frac{V}{m} \qquad (equation\ 9)$$

$$\alpha_N^{Li} = \frac{K_d(\mathrm{Li})}{K_d(N)} \qquad (equation\ 10)$$

Where K_d is the partitioning coefficient ($L \cdot mg^{-1}$), α_N^{Li} is the separation factor, and N represents the major ions in the FPW, which are Li^+, Na^+, Mg^{2+}, K^+ and Ca^{2+} in this study.

2.4.2 Adsorption kinetics and modelling

The Li^+ kinetics data were modelled using the pseudo-first-order (PFO) and pseudo-second-order (PSO) models, which can be described by *equations* 11 and 12, respectively:[62,63]

$$ln(q_e - q_t) = lnq_e - k_1 t \qquad (equation\ 11)$$

$$\frac{t}{q_t} = \frac{1}{k_2 q_e^2} + \frac{t}{q_e} \qquad (equation\ 12)$$

Where q_e and q_t are the uptakes ($mg \cdot g^{-1}$) of Li^+ at equilibrium and time t (min), respectively, and k_1(min^{-1}) and k_2($g \cdot mg^{-1} \cdot min^{-1}$) are the pseudo first-order and second-order rate constants, respectively.

An adsorption process typically comprises three sequential steps, as outlined below: (1) the adsorbate transfers from the bulk solution to the boundary film, and then to the surface of the adsorbent (also referred to as the external mass transfer step), (2) the adsorbate moves from the surface of the adsorbent to an intraparticle active site or a binding site (known as the intraparticle diffusion step), and (3) the adsorbate adsorbs onto the active sites of the adsorbent.[62,63] Generally, an adsorption process is controlled by external mass diffusion, intraparticle diffusion or both because the third step is relatively rapid, and thus cannot be treated as a rate-limiting step.[62,63] To determine possible diffusion mechanisms within the adsorption system, the intraparticle diffusion model was applied and can be described by *equation* 13:[62,63]

$$q_t = k_n t^{0.5} + C_n \qquad (equation\ 13)$$

Where k_n(mg·g^{-1}·min$^{-0.5}$) is the intraparticle diffusion rate constant of each step (n = 1, 2, 3) determined from the slope of the plot q_t versus $t^{0.5}$.

3. Results and discussions

3.1 Characterization of LMO/HMO and LMMOs/ HMMOs

SEM and TEM images of LMO and LMMO-0.4 show that the morphologies of the two adsorbents are similar in that they are composed of dispersed, cubic-like nanoparticles aggregating as floccules (Figure 7). Nanoparticle sizes of these two adsorbents range from 60 nm to 110 nm; LMMO has a slightly larger particle size than LMO. The crystallinity of LMMO-0.4 appears to be higher than that of LMO, likely because LMMO-0.4 has been calcined twice during synthesis. LMO has an interplanar spacing (*d*) of 0.47 nm in the (1 1 1) plane, and magnesium doping has no effect on this value for LMMO-0.4.

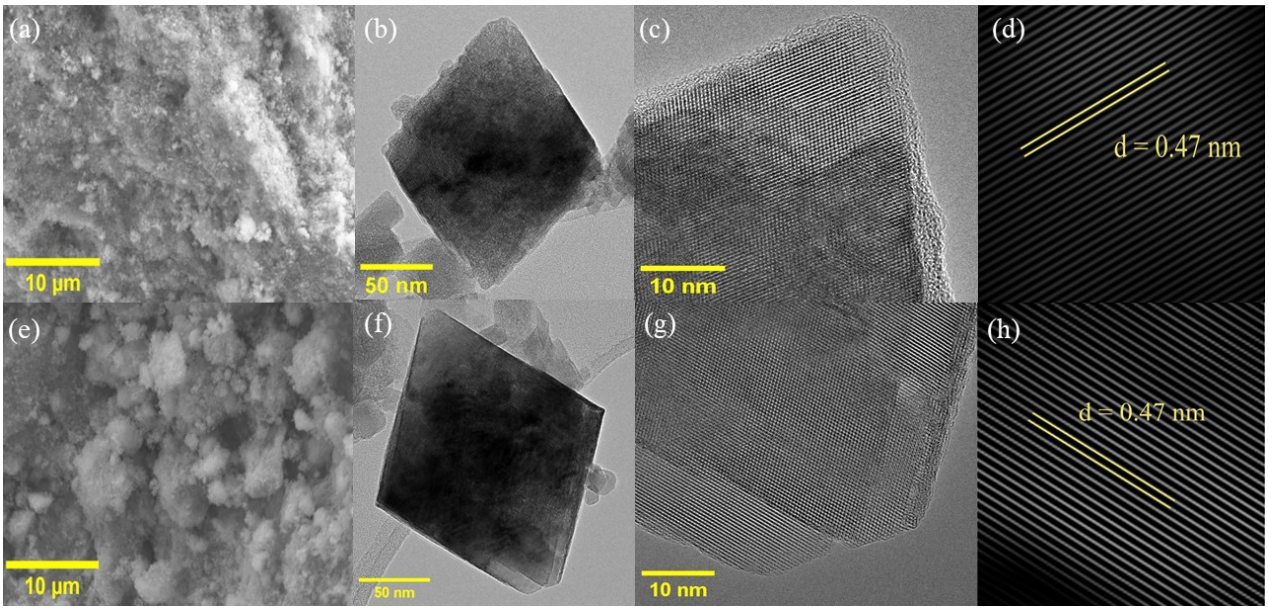

Figure 7: (a) SEM image of LMO; (b), (c) and (d) TEM images of LMO; (e) SEM image of LMMO-0.4; (f), (g) and (h) TEM images of LMMO-0.4.

Figure 8 shows the TGA curves for HMO and HMMO-x (x = 0.1-0.4). The results show that the thermal stability of the phase increases with increasing magnesium doping amount. Mass loss below 100°C is associated with the evaporation of structural water.[1,44,64] This mass loss, centered around 200-220°C, can be attributed to the dissipation of water by the condensation of

hydroxyl (-OH) groups, in conjunction with a phase transformation of the H^+-form spinel to β-MnO_2.[1,44] The mass loss between 100 and 350°C indicates the presence of structural protons in the adsorbents,[64] which were inserted into the crystal structure via ion-exchange reactions that replaced lithium with protons. These data were used to determine the total proton content of the protonated samples. Within this temperature range, the adsorbents exhibited a progressive decline in mass loss as the amount of magnesium doping increased, which implies a decrease in structural protons with increasing Mg incorporation. The structural proton contents were 8.62%, 6.34%, 4.49%, 2.46% and 1.67% for HMO, HMMO-0.1, HMMO-0.2, HMMO-0.3, and HMMO-0.1, respectively, as evaluated from the TGA curves, which were further used to determine the chemical formulas of the protonated absorbents. The TGA results confirm that magnesium doping aids in stabilizing the structures, accompanied by a reduction in the number of ion exchange sites.

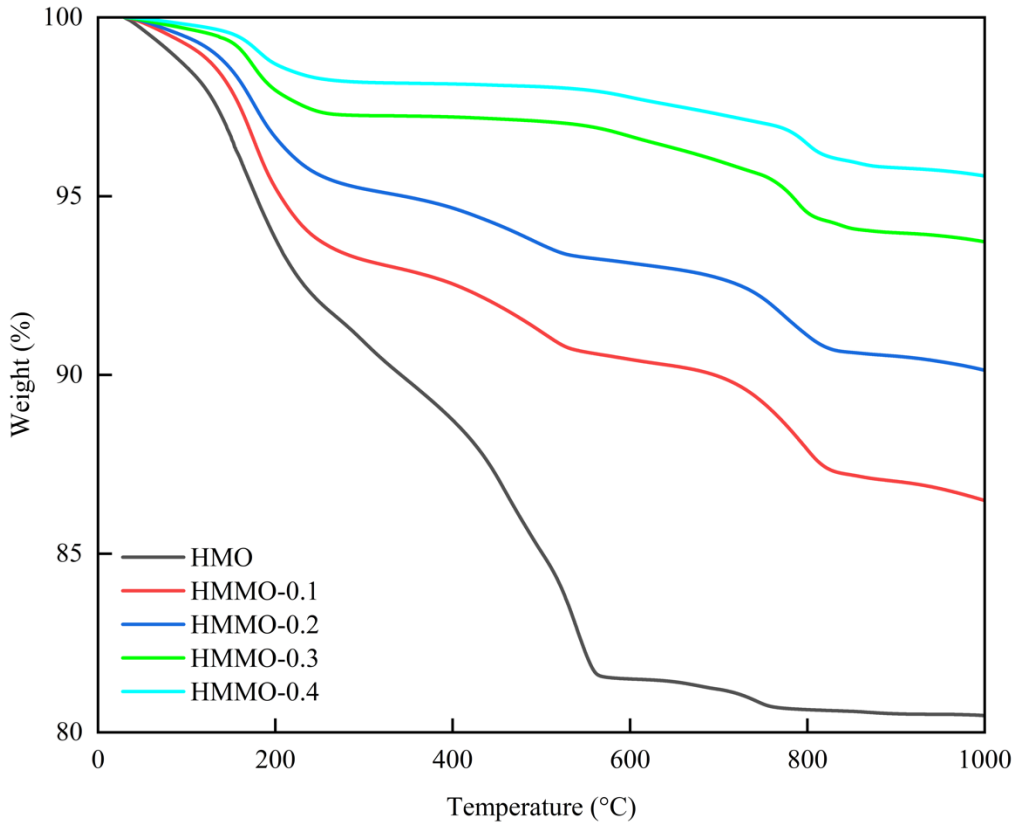

Figure 8: TGA curves of protonated samples HMO and HMMO-x (x = 0.1-0.4).

Table 2 summarizes the physical and chemical characteristics of LMO, LMMOs, and their protonated products. The values of the average manganese valence state, Z_{Mn}, in the precursors increased with greater magnesium doping, rising from 3.80 for LMO to 3.84 for LMMO-0.4. This suggests that some amount of Mn^{3+} in the lattice was substituted by Mg^{2+}. The chemical formula of LMO was determined to be $Li_{1.66}Mn_{1.66}O_4$, indicating it to be a pure ion-exchange type adsorbent.[3,36,42,65,66] Similarly, the chemical formulas of LMMOs conformed to the general formula $Li_{1.66}Mg_xMn_{1.66-x}O_4$.[36,42] HMO and HMMOs exhibited Z_{Mn} values exceeding 4.00, consistent with the Z_{Mn} of pure ion-exchange type adsorbents. Notably, the residual lithium (Li/Mn) content in the protonated samples increases with an increase in magnesium doping amount from 0.06 for HMO to 0.64 for HMMO-0.4 This trend aligns with the total proton contents determined through TGA, signifying a decrease in the number of ion exchange sites within the adsorbents. This phenomenon could be explained by structural stabilization facilitated through magnesium doping.

Table 2: Physical and chemical characteristics of LMO/HMO and LMMOs/HMMOs.

Adsorbents	**Z_{Mn}**	**Li/Mn**	**H/Mn**	**Chemical Formula**
LMO	3.80	1.00		$Li_{1.66}Mn_{1.66}O_4$
HMO	4.02	0.06	0.93	$Li_{0.10}H_{1.48}Mn_{1.60}O_4$
LMMO-0.1	3.82	1.06		$Li_{1.66}Mg_{0.10}Mn_{1.56}O_4$
HMMO-0.1	4.01	0.30	0.71	$Li_{0.47}H_{1.12}Mg_{0.12}Mn_{1.57}O_4$
LMMO-0.2	3.83	1.14		$Li_{1.64}Mg_{0.22}Mn_{1.44}O_4$
HMMO-0.2	4.01	0.47	0.57	$Li_{0.74}H_{0.84}Mg_{0.22}Mn_{1.47}O_4$
LMMO-0.3	3.84	1.15		$Li_{1.56}Mg_{0.33}Mn_{1.36}O_4$
HMMO-0.3	4.01	0.61	0.40	$Li_{0.95}H_{0.53}Mg_{0.33}Mn_{1.33}O_4$
LMMO-0.4	3.84	1.25		$Li_{1.57}Mg_{0.43}Mn_{1.26}O_4$
HMMO-0.4	4.02	0.64	0.33	$Li_{1.08}H_{0.41}Mg_{0.42}Mn_{1.26}O_4$

3.2 Adsorption and desorption

3.2.1 Performance in FPW

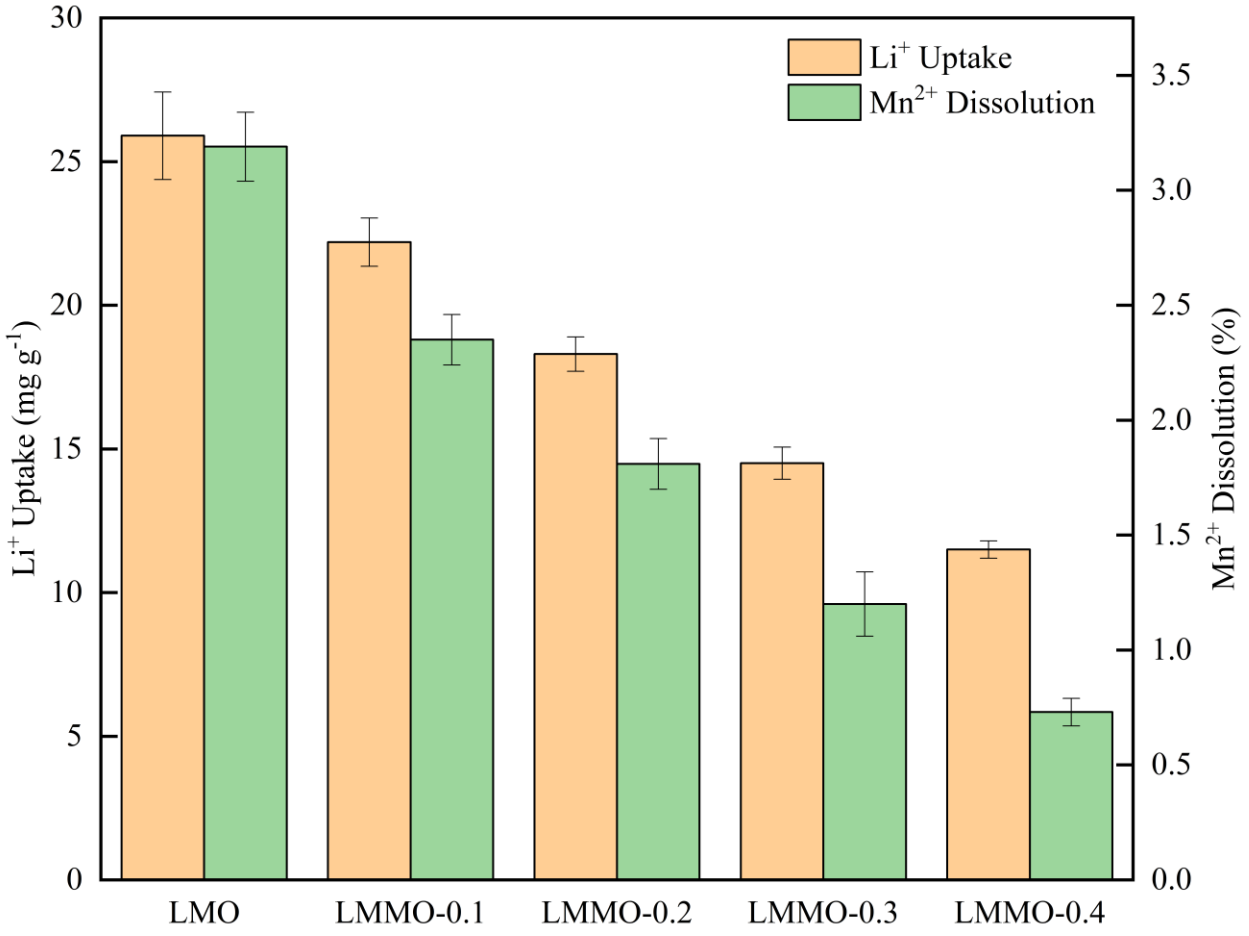

Figure 9: Li^+ uptakes of the adsorbents applied to FPW, and Mn^{2+} dissolutions from the adsorbents when exposed to 0.1 M H_2SO_4 during the subsequent delithiation step.

Figure 9 compares the Li^+ uptakes from FPW for the 5 types of ion exchange adsorbents, and shows Mn^{2+} loss from the same adsorbents when exposed to 0.1 M H_2SO_4 during the delithiation step that follows. The Li^+ uptake exhibits a gradual decline, decreasing from 25.7 $mg \cdot g^{-1}$ for HMO to 11.3 $mg \cdot g^{-1}$ for HMMO-0.4. This reduction in Li^+ uptake corresponds consistently with the total proton content determined for each adsorbent through TGA measurements. On the other hand, the average Mn^{2+} dissolution decreases significantly from 3.19% for LMO to 0.73% for LMMO-0.4. The results confirm that doping with magnesium can effectively inhibit Mn^{2+}

dissolution while simultaneously reducing the Li^+ uptake because the substitution of Mn^{3+} by Mg^{2+} reduces the content of structural Mn^{3+}, further leading to a reduction in the number of ion exchange sites. Despite the diminishing Li^+ uptake seen in LMMOs, their significantly reduced Mn^{2+} dissolution makes them viable materials for recovering Li from FPW, as the reductive dissolution of Mn is among the most pressing problems in the reuse of LMOs. Indeed, the Li^+ uptake 11.3 $mg \cdot g^{-1}$ for HMMO-0.4 remains relatively high compared to other DLE adsorbents.

3.2.2 Adsorption kinetics

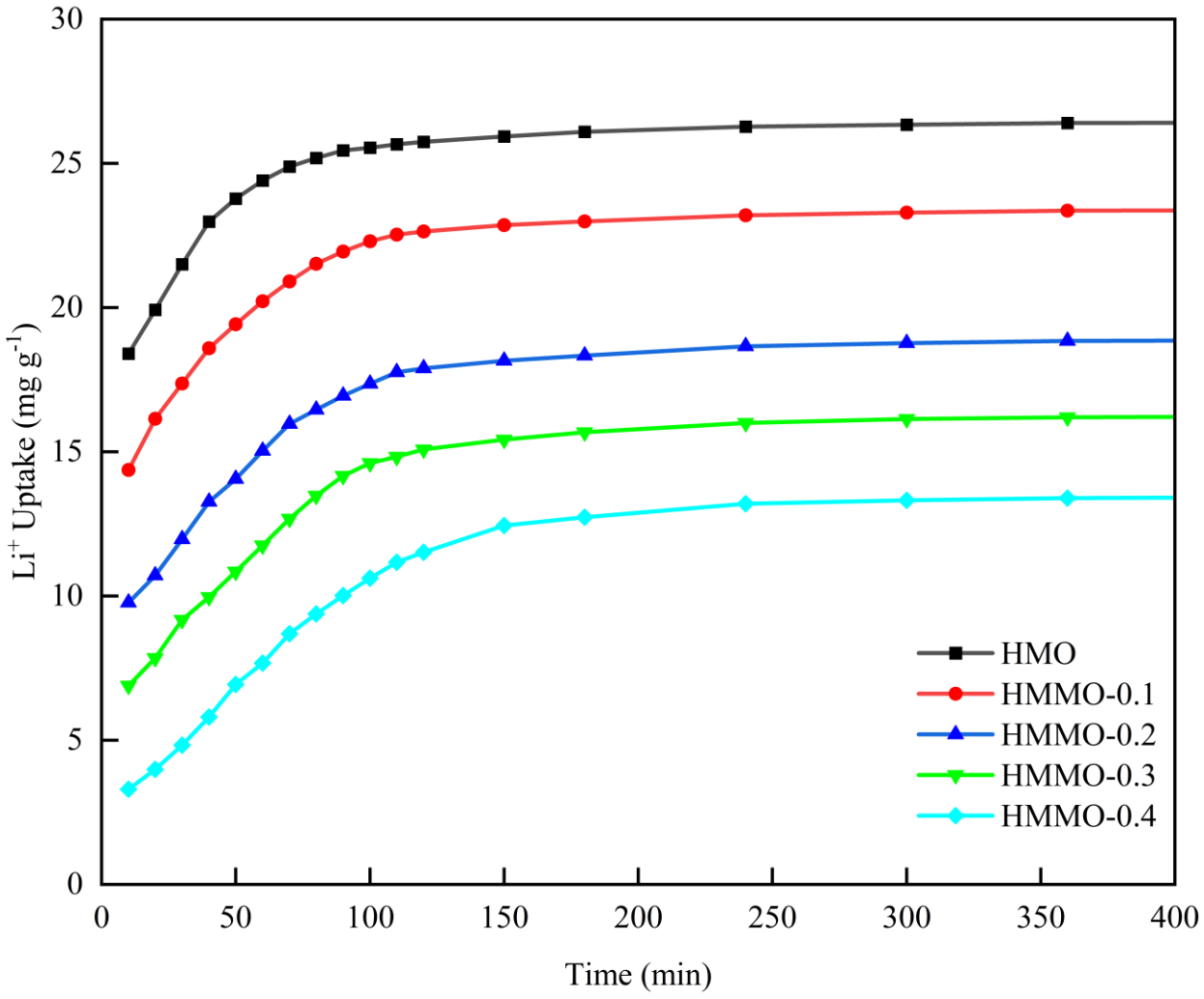

Figure 10: Li^+ uptake kinetics of the adsorbents in FPW adjusted to pH 8.

In order to investigate the effects of various levels of magnesium doping on Li^+ uptake, Li^+ adsorption kinetics experiments were performed in FPW adjusted to pH 8. The results of Li^+ adsorption kinetics experiments are shown in Figure 10. Li^+ uptake increases during the initial stage, reaching plateaus that represent near-maximum uptake at approximately 90, 100, 110, 120 and 150 minutes for HMO, HMMO-0.1, HMMO-0.2, HMMO-0.3 and HMMO-0.4, respectively. After 120 minutes of reaction, Li^+ adsorption to HMO, HMMO-0.1, HMMO-0.2, HMMO-0.3, and HMMO-0.4 reach 97.3%, 96.5%, 94.4%, 92.3% and 84.7% of their equilibrium Li^+ uptakes, respectively. Therefore, 120 minutes was chosen as the Li^+ adsorption time throughout this study.

3.2.3 Adsorption kinetics modelling

Li^+ adsorption kinetics were evaluated using three commonly employed models: the pseudo-first-order (PFO) model, the pseudo-second-order (PSO) model, and the intraparticle diffusion model. The fitting results for these models are depicted in Figure 11. Detailed fitting parameters are given in Table 3.

LMMOs exhibit slower Li^+ uptake rates, as evident from the continuous decrease in rate constants, k_1 and k_2, with increasing magnesium doping. The modeling shows better fitting outcomes with the PSO model ($R^2 > 0.99812$) than the PFO model ($R^2 > 0.87103$), indicating that the Li^+ adsorption process is dominated by chemical adsorption or chemisorption of Li^+ onto active sites of the adsorbents due to valency forces.[67,68] Moreover, the calculated equilibrium Li^+ uptakes derived from the PSO model are in good agreement with the experimental values.

The intraparticle diffusion model reveals three linear segments (Figure 11c). Because the first linear regression segments deviate from the origin, indicating the process of Li^+ adsorption is influenced by multiple mechanisms rather than being solely controlled by intraparticle diffusion.[67,68] The initial stage, which occurs within the first 10 minutes, has the most rapid lithium

mass transfer as shown by the steep slope. During this phase, Li^+ migrates from the bulk fluid-phase water (FPW) to the interfacial boundary film and subsequently to the surface of the adsorbents. The second stage of lithium uptake is more gradual, as indicated by the second linear segment of the kinetics fit, and signifies intraparticle diffusion where Li^+ travels from the adsorbent surface into active ion exchange sites within the particle structure. Finally, the concluding stage, with a nearly horizontal linear trend, represents the attainment of equilibrium. This model demonstrates that Li^+ adsorption is controlled by both external mass transfer and intraparticle diffusion.[60,61,67,68]

Table 3: Rate parameters of the adsorbents for PSO, PFO and intraparticle models.

Adsorbent	$q_{e,exp}$ (mg g^{-1})	Pseudo first-order model			Pseudo second-order model			Intraparticle model		
		$q_{e,cal}$ (mg g^{-1})	k_1 (min^{-1})	R^2	$q_{e,cal}$ (mg g^{-1})	k_2 (g mg^{-1} min^{-1})	R^2	k_1 (mg g^{-1} $min^{0.5}$)	k_2 (mg g^{-1} $min^{0.5}$)	k_3 (mg g^{-1} $min^{0.5}$)
HMO	26.47	2.26	0.00632	0.87724	26.59	0.00828	0.99998	5.6052	1.1844	0.1010
HMMO-0.1	23.46	2.97	0.00631	0.87967	23.63	0.00586	0.99994	4.3565	1.1326	0.0971
HMMO-0.2	18.96	3.69	0.00625	0.88563	19.18	0.00438	0.99983	3.0621	1.1761	0.1190
HMMO-0.3	16.35	3.96	0.00597	0.88114	16.63	0.00354	0.99963	2.0298	1.1454	0.1146
HMMO-0.4	13.60	5.11	0.00570	0.87103	14.14	0.00183	0.99812	1.3530	0.9759	0.1155

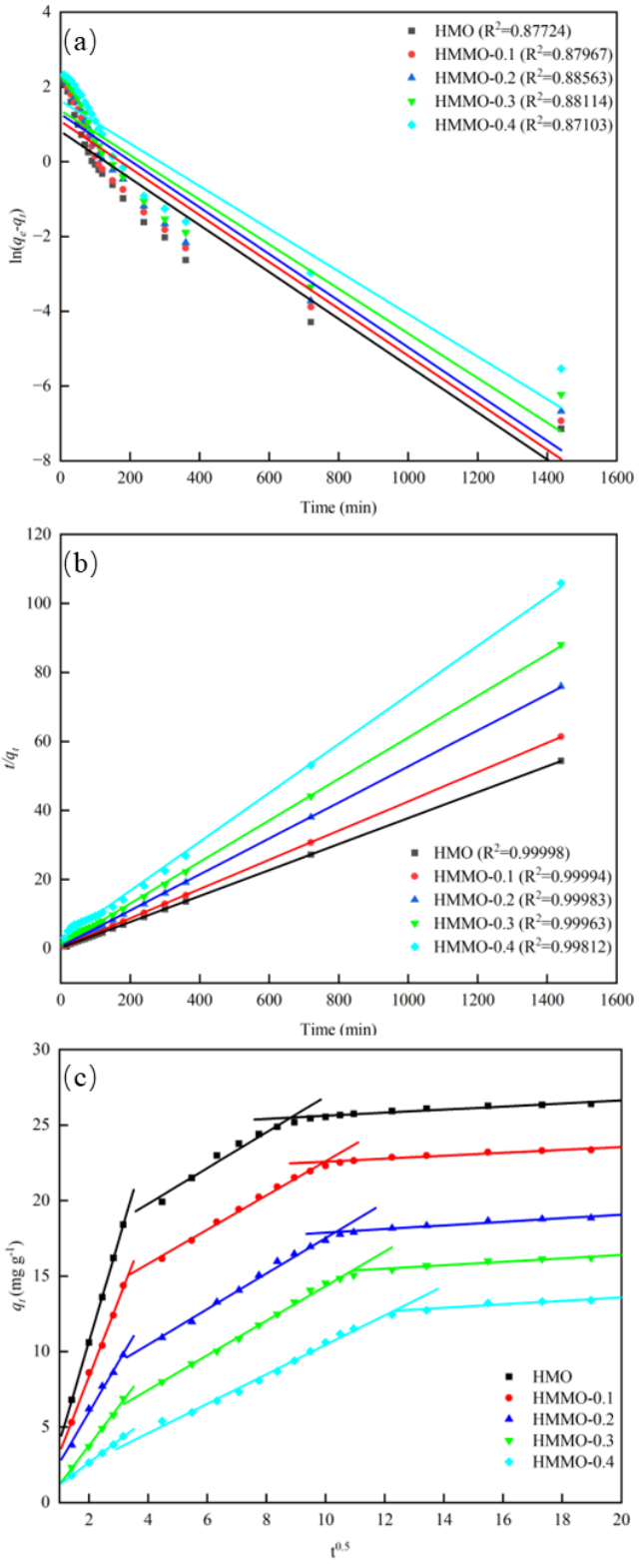

Figure 11: (a) Pseudo-first-order, (b) pseudo-second-order, and (c) intraparticle diffusion models for Li^+ adsorption kinetics.

3.2.4 Adsorption selectivity

The presence of high concentrations of co-existing ions in FPW can have a significant effect on Li^+ uptake from solution. The selectivity parameters of HMMO-0.4 in FPW, which show the ability of HMMO-0.4 to preferentially adsorb Li^+ over others from FPW, are shown in Table 4. The Li^+ uptake at equilibrium is 13.6 $mg \cdot L^{-1}$, whereas the uptakes of other ions are comparatively low (< 1.3 $mg \cdot L^{-1}$ for Mg^{2+}). This observation underscores the remarkable selectivity of HMMO-0.4 for Li^+, with its selective order determined to be $Li^+ > Mg^{2+} > K^+ > Na^+ > Ca^{2+}$. Similar results were also found with other HMMOs and HMO (Table A1-A4). This high selectivity of Li^+ can be attributed to the size similarity between the ionic radius of Li^+ (0.069 nm) and the ion exchange sites of the adsorbents.[43] LMMOs are synthesized in the presence of Li^+, enabling the size of ion exchange sites precisely matches that of Li^+. Consequently, Li^+ is the primary ion found in FPW capable of occupying the ion exchange sites within LMO and LMMOs despite the presence of high concentrations of other ions. Interestingly, despite the close ionic radius of Mg^{2+} (0.072nm) to that of Li^+, HMMOs are not selective to Mg^{2+} due to a higher dehydration energy needed for Mg^{2+}, making its incorporation into HMMOs less favorable.[43] Compared to HMO (Table A1), the K_d values of Li^+ for HMMOs (Table A2-A3) decrease with the increase in Mg^{2+} doping due to the decrease in Li^+ uptakes for HMMOs. The selectivity test demonstrates that HMMOs are highly selective materials for lithium recovery from high TDS brines, including FPW.

Table 4: Selectivity parameters of HMMO-0.4 in FPW.

Parameter	Major ions				
	Li^+	Na^+	Mg^{2+}	K^+	Ca^{2+}
ρ_i (mg·L^{-1})	70.2	51345.5	1225.1	2000.1	11189.3
ρ_e (mg·L^{-1})	43.0	51345.2	1222.4	1999.3	11189.3
q_e (mg·g^{-1})	13.6	0.1	1.3	0.4	0.0
$K_d \times 10^7$ (L·mg^{-1})	3176.1	0.0	10.8	2.0	0.0
α_N^{Li}	1	113528	291	1594	300769

3.2.5 Effect of acid concentration on delithiation

To determine the effects of acid concentration on delithiation, Li^+ desorption was conducted on the 1st lithiated LMMO-0.4 in both 0.1 M and 0.5 M H_2SO_4. The Li^+ stripping efficiency curves in Figure 12 mostly overlap, indicating that the concentration of the stripping acid has minimal influence on Li^+ stripping efficiency. Li^+ desorption in the acid is rapid, with approximately 65% of the adsorbed Li^+ being released into the acid within the first 5 minutes. However, interestingly, the rate of Mn^{2+} dissolution is strongly correlated to the acid concentration. Li^+ desorption of the 1st lithiated LMMO-0.4 yields 0.93% of Mn^{2+} dissolution in 0.5 M H_2SO_4 compared to a lower value of 0.73% in 0.1 M H_2SO_4. Similar effects are also observed in the desorption of other lithiated LMMOs and LMO; Mn^{2+} dissolution is 0.67%, 0.58%, 0.37%, and 0.28% lower for LMO, LMMO-0.1, LMMO-0.2, and LMMO-0.3 when using 0.1 M H_2SO_4, respectively. This is likely because the less concentrated acid has a somewhat higher pH, which can inhibit the disproportionation reaction of Mn^{3+} as described in *equation* 1a. This discovery holds significant implications, notably reducing the financial expenses associated with the desorption acid, a critical factor in the commercial production of lithium from low-lithium bearing brines utilizing manganese-based ion exchange adsorbents.

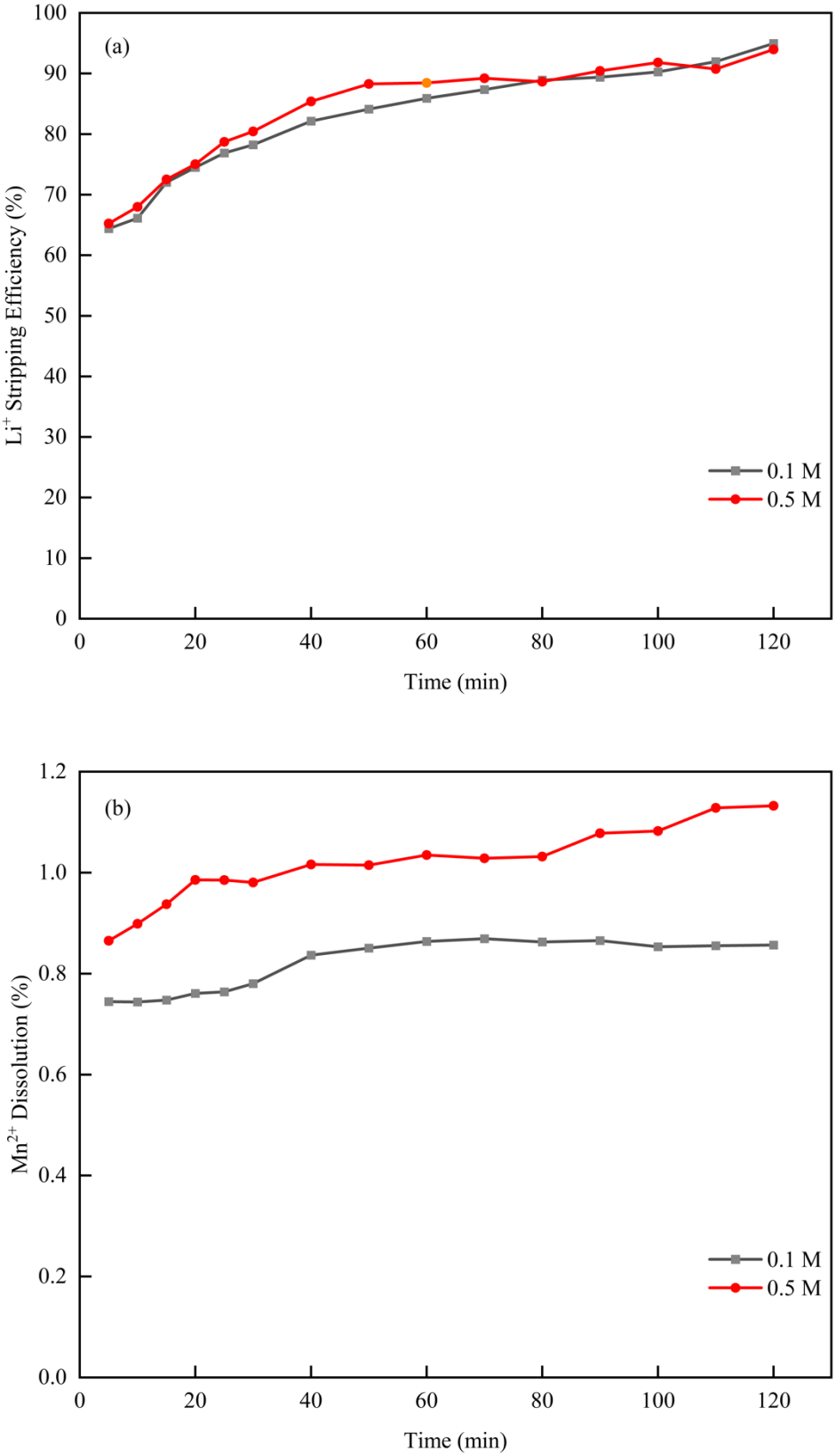

Figure 12: (a) Li^+ stripping efficiency (b) Mn^{2+} dissolution for the 1st lithiated LMMO-0.4 in 0.1 M and 0.5 M H_2SO_4.

3.2.6 Recycling of adsorbents

Ideally, an adsorbent should be capable of being reused at least a hundred times, and perhaps even several hundred times, to achieve economic viability in commercial DLE plants. Therefore, developing adsorbents with good recyclability is essential to the commercialization of lithium extraction from low lithium-bearing brines (e.g., FPW).

To assess the recyclability and durability of the LMMOs developed here when deployed for Li recovery from FPW, 5 cycles of adsorption and desorption were conducted in this study. As depicted in Figure 13, both the Li^+ uptake and Mn^{2+} dissolution from the adsorbents decline as the number of cycles increases. HMO displays a more pronounced reduction in Li^+ uptake compared to HMMOs; HMMOs retain over 95% of their initial Li^+ uptakes after the 5^{th} cycle, whereas HMO retains only 90% of its initial Li^+ uptake under the same conditions. This phenomenon can be attributed to the increased stability of HMMOs due to magnesium doping in the structure. Mn^{2+} loss from the sorbents varied from 2.81% for HMO to 0.68% for HMMO-0.4 at the 5^{th} cycle of desorption, which decrease sightly compared to the 1^{st} cycle. These cycling test results confirm that LMMOs are more stable than LMO during repeated use.

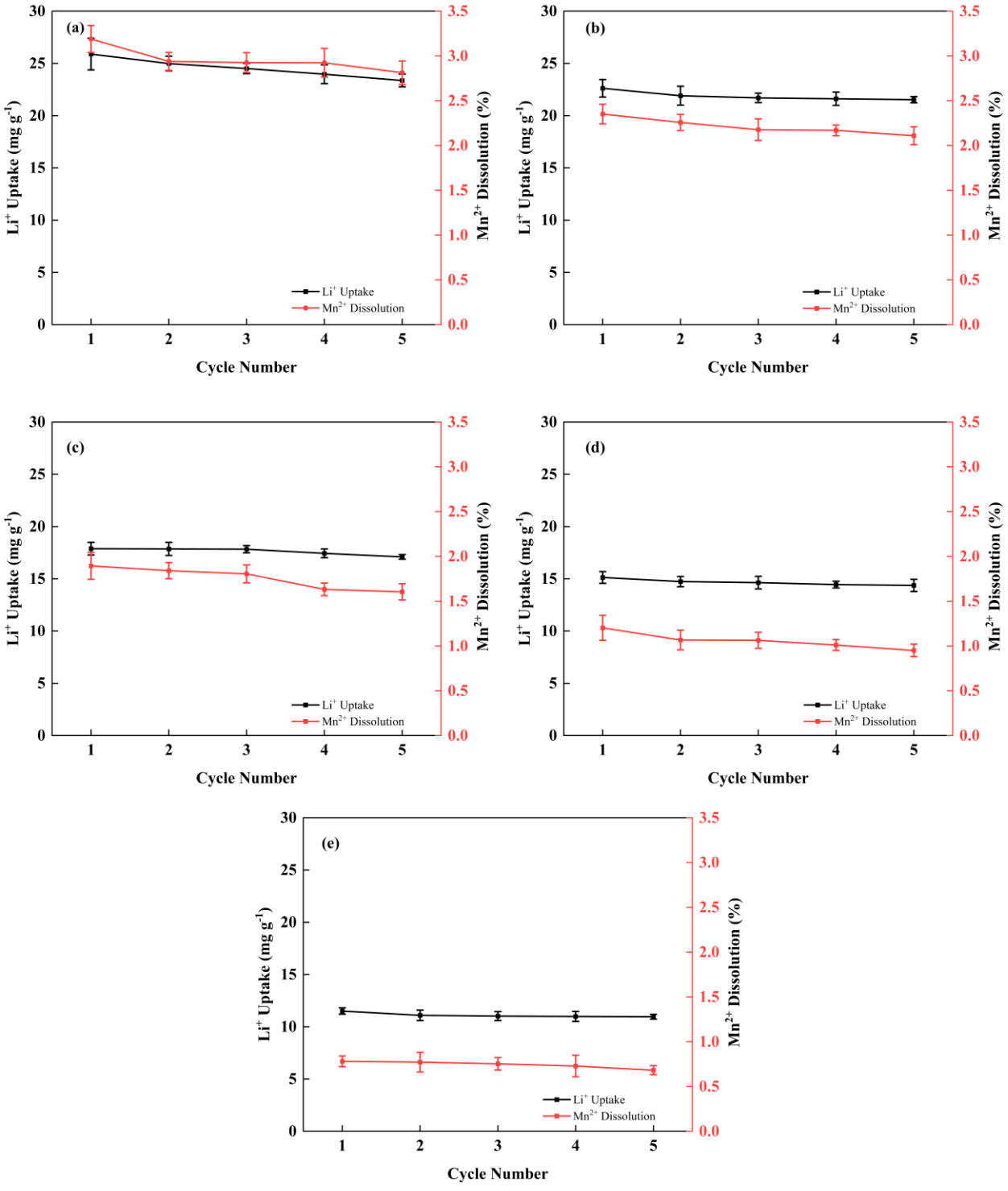

Figure 13: Li^+ uptake and Mn^{2+} dissolution from (a) LMO, (b) LMMO-0.1, (c) LMMO-0.2, (d) LMMO-0.3, and (e) LMMO-0.4 across 5 adsorption and desorption cycles.

3.3 Effects of dissolved organic compounds on adsorbent performance

3.3.1 Adsorbent performance in synthetic brine

There is evidence suggesting that the presence of dissolved organic compounds in the FPW can coat the adsorbent and induce the reduction of manganese, followed by its subsequent release into the acid during delithiation.[1] To evaluate the effect of dissolved organic compounds that are present in FPW on the performance of the adsorbents in terms of Li^+ uptake and Mn^{2+} loss, a synthetic lithium-containing brine was created with an inorganic chemistry comparable to the FPW sample studied here. To mimic the buffering capacity of FPW, sodium bicarbonate ($NaHCO_3$) was introduced into the synthetic brine.[1,43] Adsorption and desorption experiments were conducted on all adsorbents in both FPW and the synthetic brine under identical conditions. Figure 14 compares the Li^+ uptakes and Mn^{2+} loss from the adsorbents in both brines. The adsorbents had slightly higher Li^+ uptakes in the synthetic brine than in FPW. This difference could be attributed to a higher buffering capacity of the synthetic brine,[1] as evidenced by a smaller pH drop observed in synthetic brine compared to FPW at the end of the adsorption process. However, Mn^{2+} loss was significantly lower with the synthetic brine than with FPW, ranging from 0.25% for HMMO-0.4 to 0.67% for HMO. A similar result was previously reported by Seip et al.[1] More significantly, HMO exhibited a greater increase in Mn^{2+} loss compared to HMMOs when transitioning from synthetic brine to FPW, which suggests that magnesium doping enhances the ability of the adsorbents to resist manganese reduction caused by the dissolved organic compounds found in the FPW.

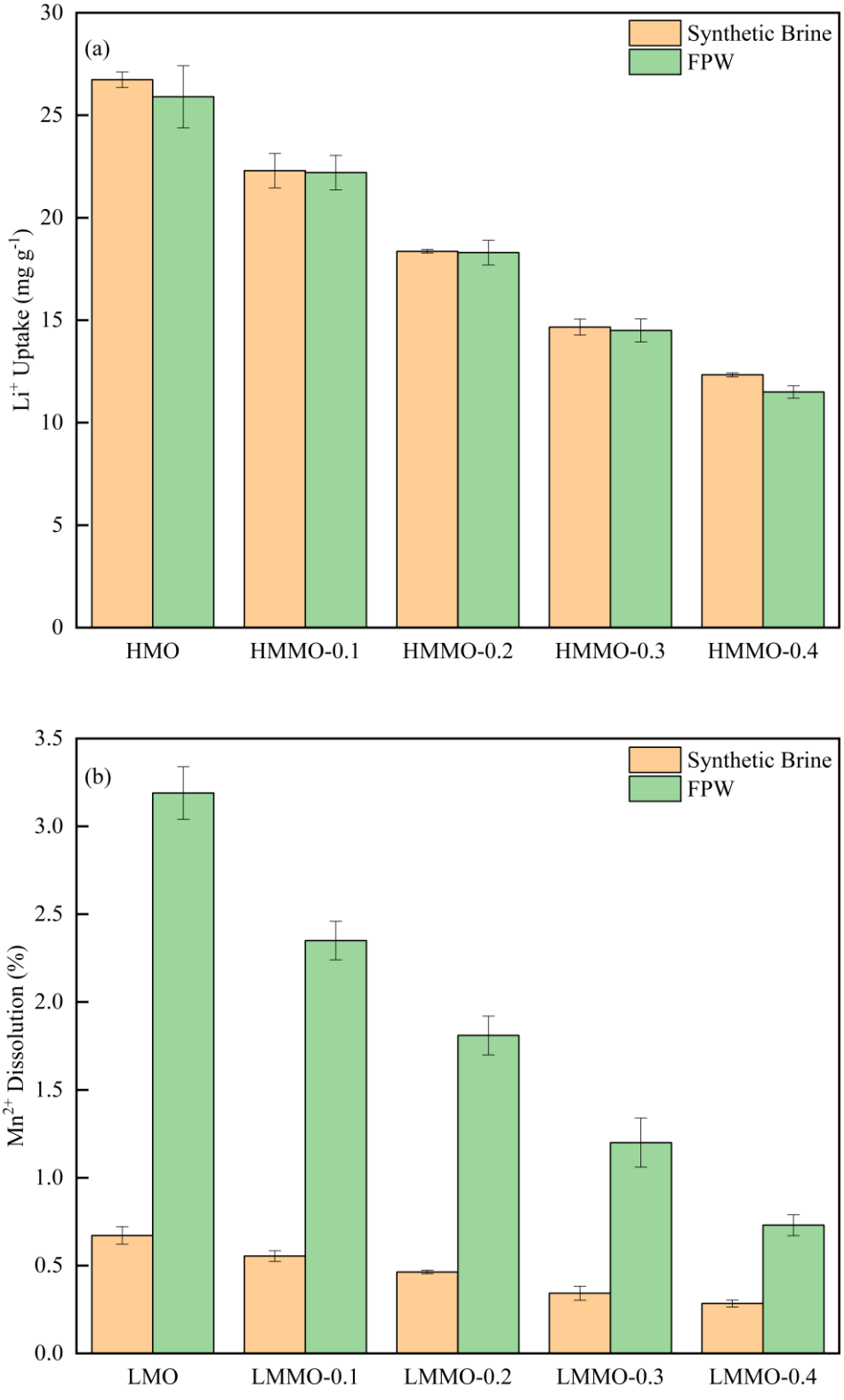

Figure 14: (a) Li^+ uptakes and (b) Mn^{2+} dissolutions from the adsorbents in both FPW and synthetic brine.

3.3.2 Manganese reduction in FPW

FPW contains a wide range of dissolved organic species which are naturally present in formation water and can also result from additives of fracturing fluids. Polyethylene glycols (PEGs), octylphenol ethoxylates (OPEs) and alkyl dimethyl benzyl ammonium chlorides (ADBACs) are the common organic species found in FPW from the Duvernay Formation in Alberta.[1,69] Additionally, FPW contains other organic components such as humic, fulvic, gallic, ascorbic, and tannic acids, all of which occur naturally and possess the ability to trigger the reduction of manganese.[1] When manganese-based adsorbents interact with these organic species, the structural manganese within them undergoes reduction, leading to its subsequent dissolution in an acidic solution.

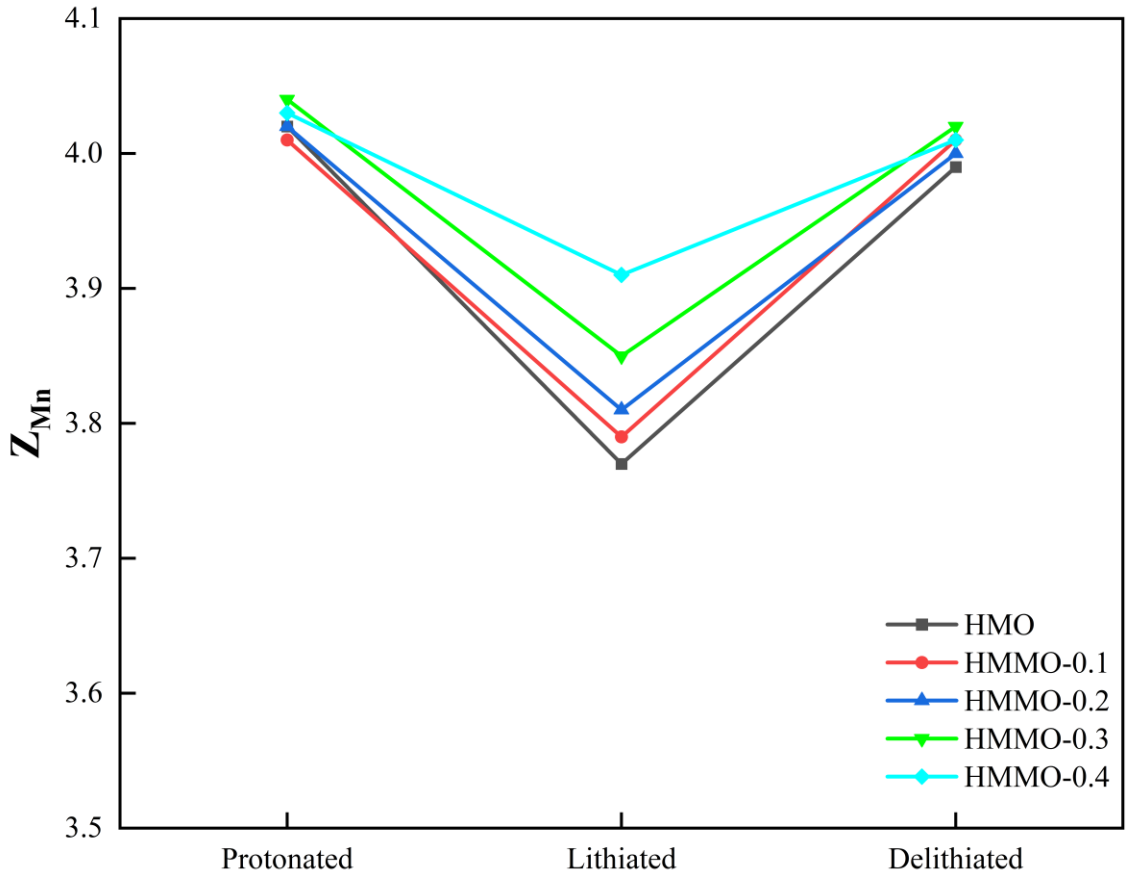

Figure 15: Changes in the average Mn valence state, Z_{Mn}, of the adsorbents through an adsorption/desorption cycle during lithium recovery from FPW.

To verify enhancement in the resistance of manganese-based adsorbents to manganese reduction in FPW following magnesium doping, lithiated and delithiated adsorbents were analyzed for Z_{Mn} by the standard oxalic acid method[1,58] Z_{Mn} of LMO experienced a significant drop from 4.02 to 3.77 after lithium adsorption in FPW (Figure 15), resulting in Mn^{2+} loss of 3.19% during acid desorption. On the other hand, lithiated LMMOs exhibited smaller drops in Z_{Mn} with FPW, ranging from 3.79 for LMMO-0.1 to 3.91 for LMMO-0.4, which correlate well with less Mn^{2+} loss (0.73-2.35%). Mn^{2+} loss from LMMO-0.4 (0.73%) following lithium recovery from FPW was comparable to that of LMO in synthetic brine (0.67%), which may suggest that magnesium doping improves the resistance of the adsorbents to Mn reduction caused by dissolved organic compounds in FPW. Subsequently, Z_{Mn} values of the adsorbents returned to nearly 4.00 after desorption.

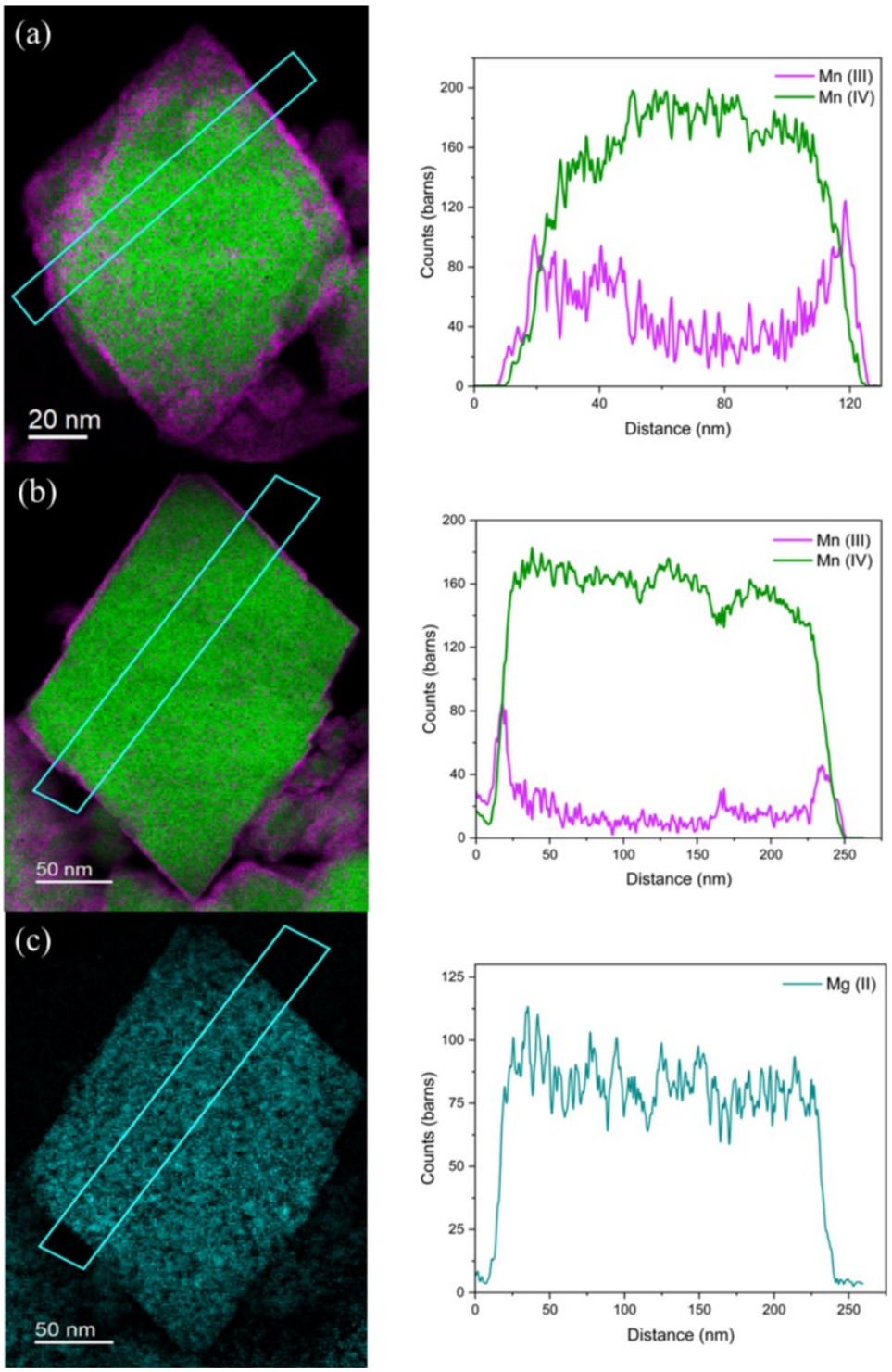

Figure 16: TEM-EELS maps (left) display spatial distribution of relative abundances of Mn^{3+} (purple), Mn^{4+} (green), Mg^{2+} (blue) in individual nanoparticles of lithiated samples including (a) LMO, (b) and (c) LMMO-0.4, both exposed to FPW. The graphs (right) display the relative abundances of Mn^{3+}, Mn^{4+} and Mg^{2+} in the blue boxed regions in the TEM-EELS maps, indicating Mn^{3+} accumulation near the particle edges and Mg^{2+} doped evenly in the structure of LMMO-0.4.

In an effort to visualize the manganese reduction caused by FPW, and to quantify the average manganese valence state in the bulk synthetic minerals, TEM-EELS analyses were carried out on lithiated samples exposed to FPW for both the LMO and LMMO-0.4 materials. EELS line scans were conducted on individual nanoparticles to visualize the spatial distributions of magnesium and manganese (in the Mn^{4+} and Mn^{3+} valence states) in the particles at the nanometer scale. EELS results show that a surface layer composed of Mn^{3+} was generated on the particle surface of both of the lithiated samples, whereas the predominant manganese valence state in the bulk phase remained mostly Mn^{4+} (Figure 16). A similar result was previously reported by Seip et al.[1] This phenomenon indicates that manganese reduction mainly happens on the surface of the absorbents, where they are directly exposed to the brine. When reduced manganese is further released in acid, contraction of the crystal structure occurs. The primary distinction noted between the two samples was that the lithium-reinserted sample of LMMO-0.4 (Z_{Mn}=3.91) contains a relatively uniform distribution of doped magnesium (Figure 16) and has a significantly lower amount of Mn^{3+} in the particle interior than LMO (Z_{Mn}=3.77), which is consistent with the measured Z_{Mn} values for these two samples. These results confirm that magnesium doping improves the ability of adsorbents to withstand manganese reduction triggered by dissolved organic compounds present in FPW.

3.4Structural analysis of adsorbents during cycling

In order to elucidate structural transformations of the manganese adsorbents as structural magnesium ions are introduced and during Li^+ adsorption/desorption cycles, synchrotron-based X-ray absorption spectroscopy (XAS) analyses were conducted. This section discusses those results in detail.

3.4.1 X-ray absorption near-edge structure (XANES)

Figure 17 displays the X-ray absorption near-edge structure (XANES) spectra at the top and their respective first derivative curves at the bottom for (a) LMO, (b) LMMO-0.2 and (c) LMMO-0.4 and their 1st lithium-reinserted, and 1st, 2nd and 5th protonated products. The letters A-D were assigned to specific energy positions within the spectra. A_1 and A_2 represent the two pre-edge peaks that commonly occur in the K-edge of most 3d elements;[70,71] these pre-edge features result from transitions to bound final states in 3d orbitals in elements like Mn.[70,71] B_1 and B_2 indicate two inflection points in the rising edge, which are typical features in spinel compounds related to medium- or long-range structural order.[70,71] The two sharp peaks, C and D, that occur after the main edge likely reflect a contraction or expansion of the crystal structure.[70,71] The positions of peaks A_1, A_2, C and D were identified from the first derivative curves at zero, whereas those of inflection points B_1 and B_2 were determined from the maxima in the first derivative curves.[70,71] The values of energy positions of the features in the XANES spectra for LMO, LMMO-0.2, LMMO-0.4 and later samples of these adsorbents taken during cycle testing are given in Tables 5, 6, and 7, respectively.

The pre-edge peaks (A_1 and A_2) of all original adsorbent materials align well in energy position compared to subsequent lithiated and delithiated adsorbent samples that were collected and analyzed during cycle testing, indicating little or no change in the local electronic structure of the manganese during adsorbent use.[70] This implies that the oxidation states of manganese for all adsorbents remains unchanged during adsorption/desorption cycling, consistent with ion exchange as the dominant lithium sorption mechanism for all the adsorbents.[70] The energy changes in the spectra of all samples show a similar pattern, in which the inflection points B_1 and B_2 on the main edges and the peaks C and D are shifted to higher energies in the protonated samples, indicating

that the protonated samples have higher manganese oxidation states.[70,71] The inflection points B_1 and B_2 exhibit greater energy shifting during adsorption/desorption cycling, which is also correlated to variations in the oxidation state of manganese,[70] while the peaks C and D show smaller displacements. The existence of the two inflection points in the magnesium doped adsorbents proves that the spinel structure is preserved.[70,71] The spectra of lithium-reinserted samples align well with spectra of the lithiated precursors, further evidence that the adsorbents are ion exchange materials.

The overall positions of the adsorption edge (B_1 and B_2) of LMMO-0.4 and subsequent lithium-reinserted samples of this material are at higher energies than those of LMMO-0.2, LMO and their lithium-reinserted samples, whereas the spectra of all protonated samples are at similar energy positions. This indicates that the manganese in LMMO-0.4 and its lithium-reinserted successors are at a higher oxidation state than for LMO, LMMO-0.2, and their lithium reinserted versions due to introduction of structural magnesium, and that all protonated samples have nearly the same oxidation state of manganese. It is clear that variations in the inflection points B_1 and B_2 diminish with increasing magnesium doping amount. Indeed, the inflection points B_1 and B_2 of LMMO-0.4 have little variation in energy during adsorption/desorption cycling, evidence that the oxidation state of manganese changes only by a small margin. These results are consistent with Z_{Mn} results determined from the standard oxalic acid method (Figure 15). Furthermore, as the amount of magnesium doping in the lattice increases, the energy variations of peaks C and D decrease during adsorption/desorption cycling of the adsorbents. This suggests that magnesium aids in structural stabilization, combined perhaps with the fact that there is a reduced lithium uptake, resulting in a lesser degree of contraction/expansion of the crystal structure during adsorption/desorption cycles.

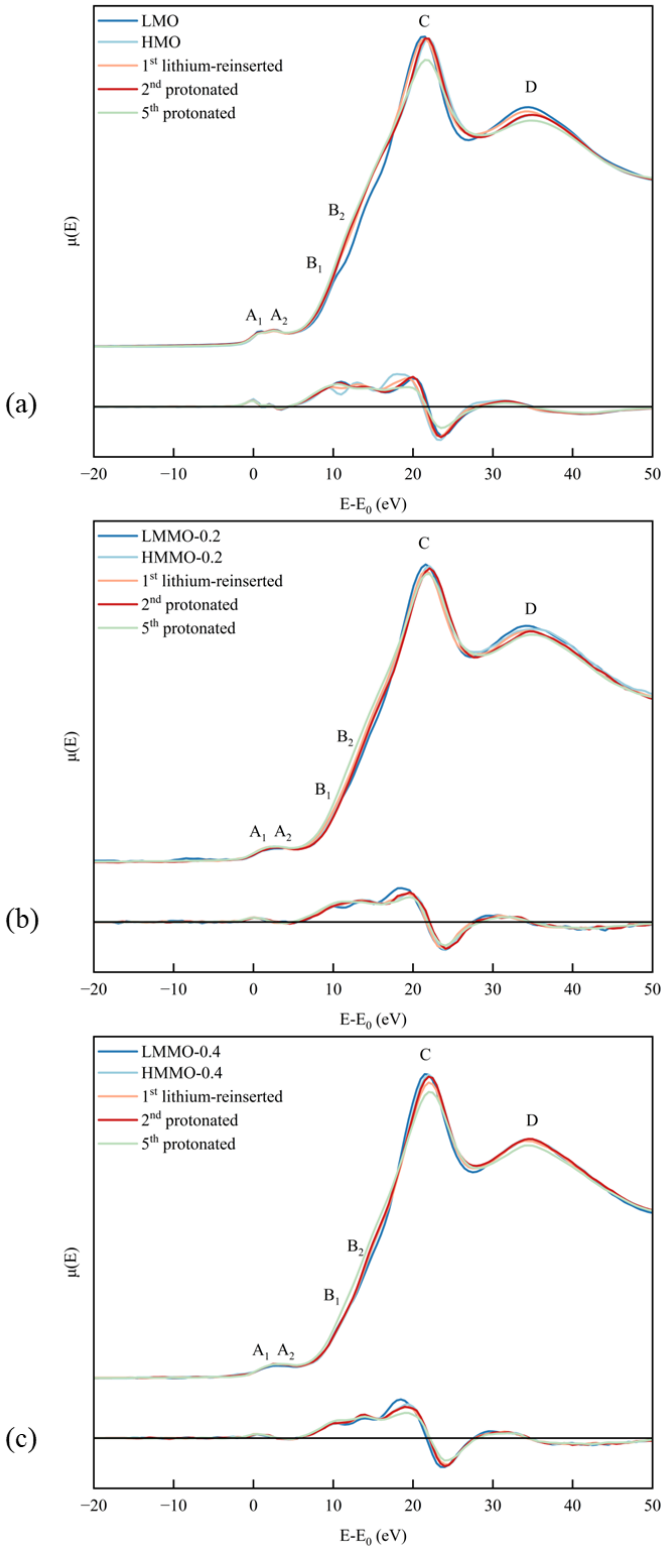

Figure 17: XANES spectra at the top and their respective first derivative curves at the bottom for (a) LMO, (b) LMMO-0.2 and (c) LMMO-0.4 and their 1st lithium-reinserted, and 1st, 2nd, and 5th protonated products.

Table 5: XANES energy positions, $E - E_0$ (eV), for LMO and its subsequent lithium-reinserted and protonated products.

Sample	A_1	A_2	B_1	B_2	C	D
LMO	1.0	2.6	9.4	13.0	21.3	34.3
HMO	1.0	2.6	11.0	14.3	22.0	34.9
1st lithium-reinserted	1.0	2.6	9.4	13.0	21.4	34.3
2nd protonated	1.0	2.6	11.0	14.3	22.0	34.9
5th protonated	1.0	2.6	11.0	14.3	22.0	34.9

Table 6: XANES energy positions, $E - E_0$ (eV), for LMMO-0.2 and its subsequent lithium-reinserted and protonated products.

Sample	A_1	A_2	B_1	B_2	C	D
LMMO-0.2	1.1	2.8	9.7	13.6	21.6	34.3
HMMO-0.2	1.1	2.8	11.2	14.2	22.0	35.1
1st lithium-reinserted	1.1	2.8	9.7	13.6	21.6	34.5
2nd protonated	1.1	2.8	11.2	14.1	22.0	35.0
5th protonated	1.1	2.8	11.2	14.1	22.0	35.0

Table 7: XANES energy positions, $E - E_0$ (eV), for LMMO-0.4 and its subsequent lithium-reinserted and protonated products.

Sample	A_1	A_2	B_1	B_2	C	D
LMMO-0.4	1.1	2.9	10.8	14.0	21.8	34.3
HMMO-0.4	1.1	2.9	11.0	14.1	22.2	34.6
1st lithium-reinserted	1.1	2.9	10.9	14.1	21.9	34.1
2nd protonated	1.1	2.9	11.0	14.1	22.2	34.4
5th protonated	1.1	2.9	11.0	14.1	22.2	34.4

3.4.2 Extended X-ray absorption fine structure (EXAFS)

The extended X-ray absorption fine structure (EXAFS) spectra and corresponding Fourier transforms of (a) LMO, (b) LMMO-0.2, and (c) LMMO-0.4 and their 1st lithium-reinserted, and 1st, 2nd, and 5th protonated products are plotted in Figure 18. The two maxima (shells) in the Fourier transforms at *ca.* 1.5 and 2.4 Å correspond to the shortest Mn-O distance of the first shell and the shortest Mn-Mn/Mg distance of the second shell, respectively.[70,71] According to the crystallographic model of lithium manganese spinel, coordination numbers were set at 6 for both shells.[70,71] The interatomic distances (R_i), i.e., Mn-O and Mn-Mn/Mg, as well as Debye-Waller factors (σ_i) of LMO, LMMO-0.2, and LMMO-0.4 were determined by curve-fitting to the experimental EXAFS data and are given in Tables 8, 9, and 10, respectively.

For all three adsorbents, the Mn-Mn/Mg distances decrease by ~0.02 Å when they are protonated, indicating a contraction of the crystal structure. This could be explained by the protonated samples containing only Mn^{4+}, as the ion radius of Mn^{4+} is smaller than that of Mn^{3+}.[71] Subsequently, the Mn-Mn/Mg distances increase, and return to close to their original values after lithium adsorption, suggesting that an expansion of the crystal structure occurs due to more Mn^{3+} present in the structure. The changes in Mn-Mn/Mg distances are consistent with the variations in the manganese oxidation state determined by the standard oxalic acid method and XANES.

The Mn-Mn/Mg distance determined for the 1st lithium-reinserted product of LMMO-0.4 is 0.01 Å smaller than those found for the 1st lithium-reinserted products of LMO and LMMO-0.2. This change correlates with the higher oxidation state of manganese in HMMO-0.4, yet further evidence that HMMO-0.4 is less susceptible to manganese reduction during lithium recovery from FPW. Another notable finding is that the 5th protonated product of LMO also shows a decrease in Mn-Mn/Mg distance when compared to the 1st and 2nd protonation steps during adsorbent cycle

testing. This suggests that an irreversible structural contraction occurred as Mn^{2+} dissolves in acid during cycles of adsorption/desorption, which is also supported by a significant reduction in Li^{+} uptake of HMO at the 5th cycle of adsorption. On the other hand, such effect is not observed in the 5th protonation cycles of LMMO-0.2 and LMMO-0.4, proving that these structures are stabilized by magnesium doping.

Table 8: Structural parameters determined from EXAFS for LMO and subsequent lithium-reinserted and protonated products.

	Mn-O		Mn-Mn/Mg	
	R_1 (Å)	σ_1 (Å)	R_2 (Å)	σ_2 (Å)
LMO	1.9	0.001	2.89	0.005
HMO	1.9	0.006	2.87	0.006
1st lithium-reinserted	1.9	0.004	2.89	0.007
2nd protonated	1.9	0.004	2.87	0.010
5th protonated	1.9	0.006	2.86	0.010

Table 9: Structural parameters determined from EXAFS for LMMO-0.2 and subsequent lithium-reinserted and protonated products.

	Mn-O		Mn-Mn/Mg	
	R_1 (Å)	σ_1 (Å)	R_2 (Å)	σ_2 (Å)
LMMO-0.2	1.9	0.002	2.89	0.004
HMMO-0.2	1.9	0.003	2.87	0.006
1st lithium-reinserted	1.9	0.005	2.89	0.008
2nd protonated	1.9	0.004	2.87	0.007
5th protonated	1.9	0.003	2.87	0.007

Table 10: Structural parameters determined from EXAFS for LMMO-0.4 and subsequent lithium-reinserted and protonated products.

	Mn-O		Mn-Mn/Mg	
	R_1 (Å)	σ_1 (Å)	R_2 (Å)	σ_2 (Å)
LMMO-0.4	1.9	0.002	2.89	0.005
HMMO-0.4	1.9	0.003	2.87	0.005
1st lithium-reinserted	1.9	0.004	2.88	0.009
2nd protonated	1.9	0.002	2.87	0.005
5th protonated	1.9	0.003	2.87	0.006

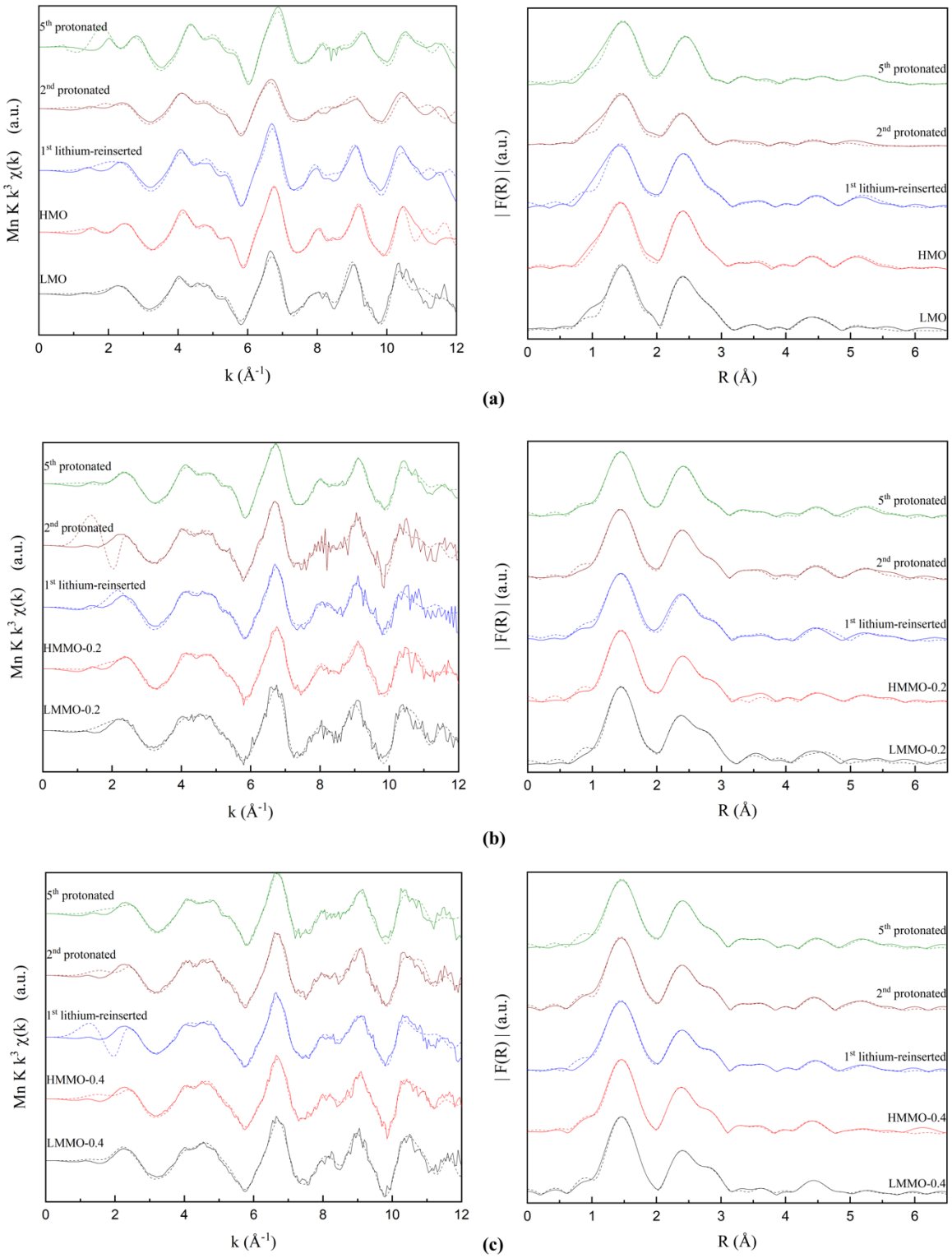

Figure 18: Mn K-edge EXAFS and corresponding Fourier transforms for (a) LMO, (b) LMMO-0.2, (c) LMMO-0.4, and their 1st lithium-reinserted, 1st, 2nd, and 5th protonated products. Dashed lines represent fits for each material.

4. Conclusions

Given the increasing global demand for lithium, driven by the recent surge in the lithium-ion battery industry, FPW is among the promising potential alternative sources of lithium. While LMO stands out as one of the most promising materials for lithium recovery from FPW, it experiences mass loss due to the reductive dissolution of manganese. In this study, a series of magnesium-doped LMMO-x (where x = 0.1, 0.2, 0.3, 0.4), or LMMOs, was synthesized by a solid-state method, aiming to solve the problem of ion-sieve mass loss by stabilizing the synthetic spinel. Adsorbent testing in FPW shows that the lithium uptake decreases with increasing magnesium doping amount, ranging from 25.7 $mg \cdot g^{-1}$ for HMO containing no Mg, to 11.3 $mg \cdot g^{-1}$ for HMMO-0.4. While this loss in lithium uptake is not desirable, the average manganese dissolution decreases dramatically from 3.19% for LMO to 0.73% for LMMO-0.4 in the subsequent acid desorption step. The substantial decrease in manganese dissolution indicates an enhancement in the stability of LMMOs, rendering them promising materials for scaling up commercialization of lithium production, as stability of DLE materials is essential for the process to be commercially viable. Lithium adsorption by these absorbents is found to follow a PSO kinetics model, and LMMOs show considerably slower lithium uptake rates with increasing Mg doping. Cycling testing shows that LMMOs retain 95% of their initial lithium uptake after the 5^{th} cycle of use, compared to only 90% for LMO, proving that LMMOs are more stable and exhibit better recyclability due to the magnesium doping. The increased stability of LMMOs was further evidenced by EXAFS spectroscopy analyses. In EXAFS, a reduction in the Mn-Mn distance in the HMO sample occurred following the 5^{th} protonation step, suggesting that irreversible structural contraction occurs as more Mn is lost during cycling. This effect is not apparent in the HMMOs samples. Consequently, HMO experiences a more significant decline in its Li^+ uptake compared to HMMOs.

This indicates that doping with magnesium helps to stabilize the structure of the adsorbents during recycling. This study demonstrates conclusively that LMMOs are promising candidates for lithium recovery from FPW.

5. Future work

Based on the experiments conducted in this study, I have the following recommendations for future work aimed at improving the practicality of manganese-based adsorbents in lithium recovery:

1. Due to the powdery nature of nanoparticles, these ion-exchange adsorbents cannot be directly applied to industrial applications. Future studies should focus on investigating composite materials of these adsorbents, e.g., considering binding materials. Polyvinyl chloride (PVC), polyacrylamide (PAM), polyacrylonitrile (PAN), polyvinyl alcohol (PVA), polyvinylidene fluoride (PVDF), chitosan, and cellulose are common and inexpensive binding materials.[72] Binder-based composites of these adsorbents might be synthesized by using granulation and foaming techniques.[73]
2. Extensive research has been conducted on single cation-doped LMO for lithium recovery from low lithium-bearing brines. Future studies might investigate doping the LMO with multiple cations, aiming at reducing Mn^{2+} dissolution while maintaining a comparative Li^{+} uptake.
3. Surface coating of Li-ion batteries cathodes with an organic or inorganic protective layer has been proved to improve their lifetime and performance in battery applications. Similarly, this technology can be applied to ion-exchange materials for lithium recovery. Future studies might look at combining doping and coating, e.g., by coating the LMMOs with a thin layer of ZrO_2 or SiO_2.[3]

References

(1) Seip, A.; Safari, S.; Pickup, D. M.; Chadwick, A. V.; Ramos, S.; Velasco, C. A.; Cerrato, J. M.; Alessi, D. S. Lithium Recovery from Hydraulic Fracturing Flowback and Produced Water Using a Selective Ion Exchange Sorbent. *Chemical Engineering Journal* **2021**, *426*. https://doi.org/10.1016/j.cej.2021.130713.

(2) Tran, T.; Luong, V. T. Lithium Production Processes. In *Lithium Process Chemistry: Resources, Extraction, Batteries, and Recycling*; Elsevier Inc., 2015; pp 81–124. https://doi.org/10.1016/B978-0-12-801417-2.00003-7.

(3) Safari, S.; Lottermoser, B. G.; Alessi, D. S. Metal Oxide Sorbents for the Sustainable Recovery of Lithium from Unconventional Resources. *Applied Materials Today*. Elsevier Ltd June 1, 2020. https://doi.org/10.1016/j.apmt.2020.100638.

(4) U.S. Geological Survey. *Mineral Commodity Summaries 2018*; 2018. https://doi.org/https://doi.org/10.3133/70194932.

(5) U.S. Geological Survey. *Mineral Commodity Summaries 2023*; 2023. https://doi.org/10.3133/mcs2023.

(6) Murphy, O.; Haji, M. N. A Review of Technologies for Direct Lithium Extraction from Low Li+ Concentration Aqueous Solutions. *Frontiers in Chemical Engineering* **2022**, *4*. https://doi.org/10.3389/fceng.2022.1008680.

(7) Swain, B. Recovery and Recycling of Lithium: A Review. *Separation and Purification Technology*. Elsevier B.V. January 1, 2017, pp 388–403. https://doi.org/10.1016/j.seppur.2016.08.031.

(8) Tabelin, C. B.; Dallas, J.; Casanova, S.; Pelech, T.; Bournival, G.; Saydam, S.; Canbulat, I. Towards a Low-Carbon Society: A Review of Lithium Resource Availability, Challenges and Innovations in Mining, Extraction and Recycling, and Future Perspectives. *Minerals Engineering*. Elsevier Ltd March 15, 2021. https://doi.org/10.1016/j.mineng.2020.106743.

(9) Vera, M. L.; Torres, W. R.; Galli, C. I.; Chagnes, A.; Flexer, V. Environmental Impact of Direct Lithium Extraction from Brines. *Nature Reviews Earth and Environment*. Springer Nature March 1, 2023, pp 149–165. https://doi.org/10.1038/s43017-022-00387-5.

(10) Baudino, L.; Santos, C.; Pirri, C. F.; La Mantia, F.; Lamberti, A. Recent Advances in the Lithium Recovery from Water Resources: From Passive to Electrochemical Methods. *Advanced Science*. John Wiley and Sons Inc September 1, 2022. https://doi.org/10.1002/advs.202201380.

(11) Flexer, V.; Baspineiro, C. F.; Galli, C. I. Lithium Recovery from Brines: A Vital Raw Material for Green Energies with a Potential Environmental Impact in Its Mining and Processing. *Science of the Total Environment*. Elsevier B.V. October 15, 2018, pp 1188–1204. https://doi.org/10.1016/j.scitotenv.2018.05.223.

(12) Reich, R.; Slunitschek, K.; Danisi, R. M.; Eiche, E.; Kolb, J. Lithium Extraction Techniques and the Application Potential of Different Sorbents for Lithium Recovery from

Brines. *Mineral Processing and Extractive Metallurgy Review*. Taylor and Francis Ltd. 2022. https://doi.org/10.1080/08827508.2022.2047041.

(13) Grosjean, C.; Herrera Miranda, P.; Perrin, M.; Poggi, P. Assessment of World Lithium Resources and Consequences of Their Geographic Distribution on the Expected Development of the Electric Vehicle Industry. *Renewable and Sustainable Energy Reviews*. April 2012, pp 1735–1744. https://doi.org/10.1016/j.rser.2011.11.023.

(14) Stringfellow, W. T.; Dobson, P. F. Technology for the Recovery of Lithium from Geothermal Brines. *Energies*. MDPI October 1, 2021. https://doi.org/10.3390/en14206805.

(15) Kaunda, R. B. Potential Environmental Impacts of Lithium Mining. *Journal of Energy and Natural Resources Law* **2020**, *38* (3), 237–244. https://doi.org/10.1080/02646811.2020.1754596.

(16) Simmons, Wm. B. S.; Webber, K. L. Pegmatite Genesis: State of the Art. *European Journal of Mineralogy* **2008**, *20* (4), 421–438. https://doi.org/10.1127/0935-1221/2008/0020-1833.

(17) Bradley, D. C.; McCauley, A. D.; Stillings, L. M. *Mineral-Deposit Model for Lithium-Cesium-Tantalum Pegmatites Mineral Deposit Models for Resource Assessment Scientific Investigations Report 2010-5070-O*; 2017.

(18) Mohr, S. H.; Mudd, G. M.; Giurco, D. Lithium Resources and Production: Critical Assessment and Global Projections. *Minerals* **2012**, *2* (1), 65–84. https://doi.org/10.3390/min2010065.

(19) Tadesse, B.; Makuei, F.; Albijanic, B.; Dyer, L. The Beneficiation of Lithium Minerals from Hard Rock Ores: A Review. *Minerals Engineering*. Elsevier Ltd January 15, 2019, pp 170–184. https://doi.org/10.1016/j.mineng.2018.11.023.

(20) Kumar, A.; Fukuda, H.; Hatton, T. A.; Lienhard, J. H. Lithium Recovery from Oil and Gas Produced Water: A Need for a Growing Energy Industry. *ACS Energy Letters*. American Chemical Society June 14, 2019, pp 1471–1474. https://doi.org/10.1021/acsenergylett.9b00779.

(21) Chang, H.; Liu, B.; Crittenden, J. C.; Vidic, R. D. Resource Recovery and Reuse for Hydraulic Fracturing Wastewater in Unconventional Shale Gas and Oil Extraction. *Environmental Science and Technology*. American Chemical Society December 3, 2019, pp 13547–13548. https://doi.org/10.1021/acs.est.9b06240.

(22) Bishop, B. A.; Robbins, L. J. *Overview of Potential Lithium Sources in the WCSB*; 2023.

(23) Leece, A.; Jiang, C. *A Preliminary Techno-Economic Assessment of Lithium Extraction from Flowback and Produced Water from Unconventional Shale and Tight Hydrocarbon Operations in Western Canada*; 2023. https://doi.org/10.4095/331879.

(24) Barati, R.; Liang, J. T. A Review of Fracturing Fluid Systems Used for Hydraulic Fracturing of Oil and Gas Wells. *Journal of Applied Polymer Science*. John Wiley and Sons Inc. August 15, 2014. https://doi.org/10.1002/app.40735.

(25) Kingston, A. W.; Jiang, C.; Wang, X.; Hobbs, T. E. *Chemical Compositions of Flowback and Produced Water from the Duvernay Shale and Montney Tight Reservoir Developments in Western Canada: Potential for Lithium Resources from Wastewater*; 2023. https://doi.org/10.4095/331878.

(26) Flynn, S. L.; Von Gunten, K.; Warchola, T.; Snihur, K.; Forbes, T. Z.; Goss, G. G.; Gingras, M. K.; Konhauser, K. O.; Alessi, D. S. Characterization and Implications of Solids Associated with Hydraulic Fracturing Flowback and Produced Water from the Duvernay Formation, Alberta, Canada. *Environ Sci Process Impacts* **2019**, *21* (2), 242–255. https://doi.org/10.1039/c8em00404h.

(27) Eccles D.R.; Berhane H. *Geological Introduction to Lithium-Rich Formation Water with Emphasis on the Fox Creek Area of West-Central Alberta (NTS 83F and 83K)*; 2011.

(28) Shaffer, D. L.; Arias Chavez, L. H.; Ben-Sasson, M.; Romero-Vargas Castrillón, S.; Yip, N. Y.; Elimelech, M. Desalination and Reuse of High-Salinity Shale Gas Produced Water: Drivers, Technologies, and Future Directions. *Environmental Science and Technology*. September 2, 2013, pp 9569–9583. https://doi.org/10.1021/es401966e.

(29) Alessi, D. S.; Zolfaghari, A.; Kletke, S.; Gehman, J.; Allen, D. M.; Goss, G. G. Comparative Analysis of Hydraulic Fracturing Wastewater Practices in Unconventional Shale Development: Water Sourcing, Treatment and Disposal Practices. *Canadian Water Resources Journal* **2017**, *42* (2), 105–121. https://doi.org/10.1080/07011784.2016.1238782.

(30) Liu, D.; Zhao, Z.; Xu, W.; Xiong, J.; He, L. A Closed-Loop Process for Selective Lithium Recovery from Brines via Electrochemical and Precipitation. *Desalination* **2022**, *519*. https://doi.org/10.1016/j.desal.2021.115302.

(31) Sun, Y.; Wang, Q.; Wang, Y.; Yun, R.; Xiang, X. Recent Advances in Magnesium/Lithium Separation and Lithium Extraction Technologies from Salt Lake Brine. *Sep Purif Technol* **2021**, *256*. https://doi.org/10.1016/j.seppur.2020.117807.

(32) Zavahir, S.; Elmakki, T.; Gulied, M.; Ahmad, Z.; Al-Sulaiti, L.; Shon, H. K.; Chen, Y.; Park, H.; Batchelor, B.; Han, D. S. A Review on Lithium Recovery Using Electrochemical Capturing Systems. *Desalination*. Elsevier B.V. March 15, 2021. https://doi.org/10.1016/j.desal.2020.114883.

(33) Wang, J.; Yue, X.; Wang, P.; Yu, T.; Du, X.; Hao, X.; Abudula, A.; Guan, G. Electrochemical Technologies for Lithium Recovery from Liquid Resources: A Review. *Renewable and Sustainable Energy Reviews* **2022**, *154*. https://doi.org/10.1016/j.rser.2021.111813.

(34) Pérez-Rodríguez, S.; Fitch, S. D. S.; Bartlett, P. N.; Garcia-Araez, N. LiFePO4 Battery Material for the Production of Lithium from Brines: Effect of Brine Composition and Benefits of Dilution. *ChemSusChem* **2022**, *15* (1). https://doi.org/10.1002/cssc.202102182.

(35) Marchini, F.; Williams, F. J.; Calvo, E. J. Electrochemical Impedance Spectroscopy Study of the LixMn2O4 Interface with Natural Brine. *Journal of Electroanalytical Chemistry* **2018**, *819*, 428–434. https://doi.org/10.1016/j.jelechem.2017.11.071.

(36) Weng, D.; Duan, H.; Hou, Y.; Huo, J.; Chen, L.; Zhang, F.; Wang, J. Introduction of Manganese Based Lithium-Ion Sieve-A Review. *Progress in Natural Science: Materials International*. Elsevier B.V. April 1, 2020, pp 139–152. https://doi.org/10.1016/j.pnsc.2020.01.017.

(37) Jang, E.; Jang, Y.; Chung, E. Lithium Recovery from Shale Gas Produced Water Using Solvent Extraction. *Applied Geochemistry* **2017**, *78*, 343–350. https://doi.org/10.1016/j.apgeochem.2017.01.016.

(38) Liu, G.; Zhao, Z.; Ghahreman, A. Novel Approaches for Lithium Extraction from Salt-Lake Brines: A Review. *Hydrometallurgy* **2019**, *187*, 81–100. https://doi.org/10.1016/j.hydromet.2019.05.005.

(39) Kotsupalo, N. P.; Ryabtsev, A. D.; Poroshina, I. A.; Kurakov, A. A.; Mamylova, E. V.; Menzheres, L. T.; Korchagin, M. A. Effect of Structure on the Sorption Properties of Chlorine-Containing Form of Double Aluminum Lithium Hydroxide. *Russian Journal of Applied Chemistry* **2013**, *86* (4), 482–487. https://doi.org/10.1134/S1070427213040046.

(40) Jiang, H.; Yang, Y.; Sun, S.; Yu, J. Adsorption of Lithium Ions on Lithium-Aluminum Hydroxides: Equilibrium and Kinetics. *Canadian Journal of Chemical Engineering* **2020**, *98* (2), 544–555. https://doi.org/10.1002/cjce.23640.

(41) Zhong, J.; Lin, S.; Yu, J. Li+ Adsorption Performance and Mechanism Using Lithium/Aluminum Layered Double Hydroxides in Low Grade Brines. *Desalination* **2021**, *505*. https://doi.org/10.1016/j.desal.2021.114983.

(42) Xu, X.; Chen, Y.; Wan, P.; Gasem, K.; Wang, K.; He, T.; Adidharma, H.; Fan, M. Extraction of Lithium with Functionalized Lithium Ion-Sieves. *Progress in Materials Science*. Elsevier Ltd December 1, 2016, pp 276–313. https://doi.org/10.1016/j.pmatsci.2016.09.004.

(43) Chitrakar, R.; Makita, Y.; Ooi, K.; Sonoda, A. Magnesium-Doped Manganese Oxide with Lithium Ion-Sieve Property: Lithium Adsorption from Salt Lake Brine. *Bull Chem Soc Jpn* **2013**, *86* (7), 850–855. https://doi.org/10.1246/bcsj.20130019.

(44) Feng, Q.; Miyai, Y.; Kanoh, H.; Ooi, K. *Li+ Extraction/Insertion with Spinel-Type Lithium Manganese Oxides. Characterization of Redox-Type and Ion-Exchange-Type Sites*; 1992; Vol. 8. https://pubs.acs.org/sharingguidelines.

(45) Bao, L.; Zhang, J.; Wu, J.; Zhang, G.; Yang, Y.; Tang, W.; Xue, M. Preparation of Mg-Doped Li1.6Mn1.6O4 with Enhanced Li+ Adsorption Performance and Anti-Dissolution Properties of Mn. *Hydrometallurgy* **2022**, *209*. https://doi.org/10.1016/j.hydromet.2021.105772.

(46) Qian, F.; Zhao, B.; Guo, M.; Qian, Z.; Xu, N.; Wu, Z.; Liu, Z. Enhancing the Li+ Adsorption and Anti-Dissolution Properties of Li1.6Mn1.6O4 with Fe, Co Doped. *Hydrometallurgy* **2020**, *193*. https://doi.org/10.1016/j.hydromet.2020.105291.

(47) Qian, F.; Zhao, B.; Guo, M.; Wu, Z.; Zhou, W.; Liu, Z. Surface Trace Doping of Na Enhancing Structure Stability and Adsorption Properties of Li1.6Mn1.6O4 for Li+ Recovery. *Sep Purif Technol* **2021**, *256*. https://doi.org/10.1016/j.seppur.2020.117583.

(48) Qian, F.; Guo, M.; Qian, Z.; Zhao, B.; Li, J.; Wu, Z.; Liu, Z. Enabling Highly Structure Stability and Adsorption Performances of Li1.6Mn1.6O4 by Al-Gradient Surface Doping. *Sep Purif Technol* **2021**, *264*. https://doi.org/10.1016/j.seppur.2021.118433.

(49) Zhang, G.; Zhang, J.; Zhou, Y.; Qi, G.; Wu, Y.; Hai, C.; Tang, W. Synthesis of Aluminum-Doped Ion-Sieve Manganese Oxides Powders with Enhanced Adsorption Performance. *Colloids Surf A Physicochem Eng Asp* **2019**, *583*. https://doi.org/10.1016/j.colsurfa.2019.123950.

(50) Ryu, T.; Shin, J.; Ghoreishian, S. M.; Chung, K. S.; Huh, Y. S. Recovery of Lithium in Seawater Using a Titanium Intercalated Lithium Manganese Oxide Composite. *Hydrometallurgy* **2019**, *184*, 22–28. https://doi.org/10.1016/j.hydromet.2018.12.012.

(51) Ryu, T.; Rengaraj, A.; Haldorai, Y.; Shin, J.; Choe, S. R.; Lee, G. W.; Hwang, S. K.; Han, Y. K.; Kim, B. G.; Huh, Y. S.; Chung, K. S. Mechanochemical Synthesis of Silica-Lithium Manganese Oxide Composite for the Efficient Recovery of Lithium Ions from Seawater. *Solid State Ion* **2017**, *308*, 77–83. https://doi.org/10.1016/j.ssi.2017.05.020.

(52) Han, H. J.; Qu, W.; Zhang, Y. L.; Lu, H. D.; Zhang, C. L. Enhanced Performance of Li+ Adsorption for H1.6Mn1.6O4 Ion-Sieves Modified by Co Doping and Micro Array Morphology. *Ceram Int* **2021**, *47* (15), 21777–21784. https://doi.org/10.1016/j.ceramint.2021.04.194.

(53) Chitrakar, R.; Makita, Y.; Ooi, K.; Sonoda, A. Synthesis of Iron-Doped Manganese Oxides with an Ion-Sieve Property: Lithium Adsorption from Bolivian Brine. *Ind Eng Chem Res* **2014**, *53* (9), 3682–3688. https://doi.org/10.1021/ie4043642.

(54) Sorour, M. H.; El-Rafei, A. M.; Hani, H. A. Synthesis and Characterization of Electrospun Aluminum Doped Li1.6Mn1.6O4 Spinel. *Ceram Int* **2016**, *42* (4), 4911–4917. https://doi.org/10.1016/j.ceramint.2015.11.174.

(55) Chitrakar, R.; Makita, Y.; Ooi, K.; Sonoda, A. Magnesium-Doped Manganese Oxide with Lithium Ion-Sieve Property: Lithium Adsorption from Salt Lake Brine. *Bull Chem Soc Jpn* **2013**, *86* (7), 850–855. https://doi.org/10.1246/bcsj.20130019.

(56) Tian, L.; Ma, W.; Han, M. Adsorption Behavior of Li+ onto Nano-Lithium Ion Sieve from Hybrid Magnesium/Lithium Manganese Oxide. *Chemical Engineering Journal* **2010**, *156* (1), 134–140. https://doi.org/10.1016/j.cej.2009.10.008.

(57) Zhong, C. *Microbial Community Dynamics in the Hydraulic Fracturing Water Cycle from Two Newly Fractured Shale Gas Wells in the Duvernay Formation, Alberta*; 2017.

(58) Freeman, D. S.; Chapman7, W. G. *An Improved Oxalate Method for the Determination of Active Oxygen in Manganese Dioxide**; 1971; Vol. 96.

(59) Tian, L.; Ma, W.; Han, M. Adsorption Behavior of Li+ onto Nano-Lithium Ion Sieve from Hybrid Magnesium/Lithium Manganese Oxide. *Chemical Engineering Journal* **2010**, *156* (1), 134–140. https://doi.org/10.1016/j.cej.2009.10.008.

(60) Qian, F.; Guo, M.; Qian, Z.; Zhao, B.; Li, J.; Wu, Z.; Liu, Z. Enabling Highly Structure Stability and Adsorption Performances of Li1.6Mn1.6O4 by Al-Gradient Surface Doping. *Sep Purif Technol* **2021**, *264*. https://doi.org/10.1016/j.seppur.2021.118433.

(61) Qian, F.; Zhao, B.; Guo, M.; Wu, Z.; Zhou, W.; Liu, Z. Surface Trace Doping of Na Enhancing Structure Stability and Adsorption Properties of Li1.6Mn1.6O4 for Li+ Recovery. *Sep Purif Technol* **2021**, *256*. https://doi.org/10.1016/j.seppur.2020.117583.

(62) Hu, Q.; Pang, S.; Wang, D. In-Depth Insights into Mathematical Characteristics, Selection Criteria and Common Mistakes of Adsorption Kinetic Models: A Critical Review. *Separation and Purification Reviews*. Taylor and Francis Ltd. 2022, pp 281–299. https://doi.org/10.1080/15422119.2021.1922444.

(63) Wang, J.; Guo, X. Adsorption Kinetic Models: Physical Meanings, Applications, and Solving Methods. *Journal of Hazardous Materials*. Elsevier B.V. May 15, 2020. https://doi.org/10.1016/j.jhazmat.2020.122156.

(64) Chitrakar, R.; Makita, Y.; Ooi, K.; Sonoda, A. Synthesis of Iron-Doped Manganese Oxides with an Ion-Sieve Property: Lithium Adsorption from Bolivian Brine. *Ind Eng Chem Res* **2014**, *53* (9), 3682–3688. https://doi.org/10.1021/ie4043642.

(65) Sun, S. Y.; Xiao, J. L.; Wang, J.; Song, X.; Yu, J. G. Synthesis and Adsorption Properties of Li1.6Mn1.6O4 by a Combination of Redox Precipitation and Solid-Phase Reaction. *Ind Eng Chem Res* **2014**, *53* (40), 15517–15521. https://doi.org/10.1021/ie5004625.

(66) Xiao, J. L.; Sun, S. Y.; Wang, J.; Li, P.; Yu, J. G. Synthesis and Adsorption Properties of Li1.6Mn 1.6O4 Spinel. *Ind Eng Chem Res* **2013**, *52* (34), 11967–11973. https://doi.org/10.1021/ie400691d.

(67) Wang, J.; Guo, X. Adsorption Kinetic Models: Physical Meanings, Applications, and Solving Methods. *Journal of Hazardous Materials*. Elsevier B.V. May 15, 2020. https://doi.org/10.1016/j.jhazmat.2020.122156.

(68) Hu, Q.; Pang, S.; Wang, D. In-Depth Insights into Mathematical Characteristics, Selection Criteria and Common Mistakes of Adsorption Kinetic Models: A Critical Review. *Separation and Purification Reviews*. Taylor and Francis Ltd. 2022, pp 281–299. https://doi.org/10.1080/15422119.2021.1922444.

(69) Zhong, C.; Li, J.; Flynn, S. L.; Nesbø, C. L.; Sun, C.; Von Gunten, K.; Lanoil, B. D.; Goss, G. G.; Martin, J. W.; Alessi, D. S. Temporal Changes in Microbial Community Composition and Geochemistry in Flowback and Produced Water from the Duvernay Formation. *ACS Earth Space Chem* **2019**, *3* (6), 1047–1057. https://doi.org/10.1021/acsearthspacechem.9b00037.

(70) Ariza, M. J.; Jones, D. J.; Rozière, J.; Chitrakar, R.; Ooi, K. Probing the Local Structure and the Role of Protons in Lithium Sorption Processes of a New Lithium-Rich Manganese Oxide. *Chemistry of Materials* **2006**, *18* (7), 1885–1890. https://doi.org/10.1021/cm052214r.

(71) Ammundsen, B.; Jones, D. J.; Roziè, J.; Burns, G. R. *Effect of Chemical Extraction of Lithium on the Local Structure of Spinel Lithium Manganese Oxides Determined by X-Ray Absorption Spectroscopy*; 1996. https://pubs.acs.org/sharingguidelines.

(72) Ding, K.; Zhu, G.; Song, C.; Wang, Q.; Wang, L.; Wang, Z.; Meng, C.; Gao, C. Fabrication of Polyacrylonitrile-Li1.6Mn1.6O4 Composite Nanofiber Flat-Sheet

Membranes via Electrospinning Method as Effective Adsorbents for Li+ Recovery from Salt-Lake Brine. *Sep Purif Technol* **2022**, *284*. https://doi.org/10.1016/j.seppur.2021.120242.

(73) Marthi, R.; Smith, Y. R. Selective Recovery of Lithium from the Great Salt Lake Using Lithium Manganese Oxide-Diatomaceous Earth Composite. *Hydrometallurgy* **2019**, *186*, 115–125. https://doi.org/10.1016/j.hydromet.2019.03.011.

Appendix A

Table A1: Selectivity parameters of HMO in FPW.

Parameter	Major ions				
	Li^+	Na^+	Mg^{2+}	K^+	Ca^{2+}
ρ_i (mg·L^{-1})	70.2	51345.5	1225.1	2000.1	11189.3
ρ_e (mg·L^{-1})	17.3	51344.9	1222.0	1997.7	11189.3
q_e (mg·g^{-1})	26.5	0.3	1.5	1.2	0.0
$K_d \times 10^7$ (L·mg^{-1})	15334.2	0.1	12.6	6.0	0.0
α_N^{Li}	1	266979	1214	2550	1118556

Table A2: Selectivity parameters of HMMO-0.1 in FPW.

Parameter	Major ions				
	Li^+	Na^+	Mg^{2+}	K^+	Ca^{2+}
ρ_i (mg·L^{-1})	70.2	51345.5	1225.1	2000.1	11189.3
ρ_e (mg·L^{-1})	23.3	51345.0	1220.9	1998.5	11189.3
q_e (mg·g^{-1})	23.5	0.3	2.1	0.8	0.0
$K_d \times 10^7$ (L·mg^{-1})	10076.1	0.1	17.1	4.1	0.0
α_N^{Li}	1	197939	590	2456	1347321

Table A3: Selectivity parameters of HMMO-0.2 in FPW.

Parameter	Major ions				
	Li^+	Na^+	Mg^{2+}	K^+	Ca^{2+}
ρ_i (mg·L^{-1})	70.2	51345.5	1225.1	2000.1	11189.3
ρ_e (mg·L^{-1})	32.3	51345.1	1223.6	1999.7	11189.2
q_e (mg·g^{-1})	19.0	0.2	0.8	0.2	0.0
$K_d \times 10^7$ (L·mg^{-1})	5872.8	0.0	6.2	1.0	0.0
α_N^{Li}	1	159487	949	5875	224219

Table A4: Selectivity parameters of HMMO-0.3 in FPW.

Parameter	Major ions				
	Li^+	Na^+	Mg^{2+}	K^+	Ca^{2+}
ρ_i (mg·L^{-1})	70.2	51345.5	1225.1	2000.1	11189.3
ρ_e (mg·L^{-1})	37.5	51345.2	1224.2	1998.8	11189.3
q_e (mg·g^{-1})	16.3	0.1	0.4	0.7	0.0
$K_d \times 10^7$ (L·mg^{-1})	4359.0	0.0	3.5	3.4	0.0
α_N^{Li}	1	164024	1231	1297	604567